Global Biogeochemical Cycles

RESEARCH ARTICLE
10.1029/2019GB006230

Reduced $CaCO_3$ Flux to the Seafloor and Weaker Bottom Current Speeds Curtail Benthic $CaCO_3$ Dissolution Over the 21st Century

Olivier Sulpis[1], Carolina O. Dufour[2], David S. Trossman[3], Andrea J. Fassbender[4], Brian K. Arbic[5], Bernard P. Boudreau[6], John P. Dunne[7], and Alfonso Mucci[1]

[1]GEOTOP and Earth and Planetary Sciences Department, McGill University, Montreal, Québec, Canada, [2]Atmospheric and Oceanic Sciences Department, McGill University, Montreal, Québec, Canada, [3]Oden Institute for Computational Engineering and Sciences, University of Texas at Austin, Austin, TX, USA, [4]Monterey Bay Aquarium Research Institute, Moss Landing, CA, USA, [5]Department of Earth and Environmental Sciences, University of Michigan, Ann Arbor, MI, USA, [6]Department of Oceanography, Dalhousie University, Halifax, Nova Scotia, Canada, [7]Geophysical Fluid Dynamics Laboratory, National Oceanic and Atmospheric Administration, Princeton, NJ, USA

Key Points:
- Reduced $CaCO_3$ flux to the seafloor and weaker bottom-current speeds curtail benthic $CaCO_3$ dissolution over the 21st century
- Modeled bottom currents underestimate current meter observations by up to 90%
- Under RCP8.5, the mean calcite compensation depth may rise by ~800 m by the end of this century

Supporting Information:
- Supporting Information S1

Correspondence to:
O. Sulpis,
o.j.t.sulpis@uu.nl

Citation:
Sulpis, O., Dufour, C. O., Trossman, D. S., Fassbender, A. J., Arbic, B. K., Boudreau, B. P., et al (2019). Reduced $CaCO_3$ flux to the seafloor and weaker bottom current speeds curtail benthic $CaCO_3$ dissolution over the 21st century. *Global Biogeochemical Cycles*, *33*, 1654–1673. https://doi.org/10.1029/2019GB006230

Received 20 MAR 2019
Accepted 21 NOV 2019
Accepted article online 5 DEC 2019
Published online 10 DEC 2019

Abstract Results from a range of Earth System and climate models of various resolution run under high-CO_2 emission scenarios challenge the paradigm that seafloor $CaCO_3$ dissolution will grow in extent and intensify as ocean acidification develops over the next century. Under the "business as usual," RCP8.5 scenario, $CaCO_3$ dissolution increases in some areas of the deep ocean, such as the eastern central Pacific Ocean, but is projected to decrease in the Northern Pacific and abyssal Atlantic Ocean by the year 2100. The flux of $CaCO_3$ to the seafloor and bottom-current speeds, both of which are expected to decrease globally through the 21st century, govern changes in benthic $CaCO_3$ dissolution rates over 53% and 31% of the dissolving seafloor, respectively. Below the calcite compensation depth, a reduced $CaCO_3$ flux to the $CaCO_3$-free seabed modulates the amount of $CaCO_3$ material dissolved at the sediment-water interface. Slower bottom-water circulation leads to thicker diffusive boundary layers above the sediment bed and a consequent stronger transport barrier to $CaCO_3$ dissolution. While all investigated models predict a weakening of bottom current speeds over most of the seafloor by the end of the 21st century, strong discrepancies exist in the magnitude of the predicted speeds. Overall, the poor performance of most models in reproducing modern bottom-water velocities and $CaCO_3$ rain rates coupled with the existence of large disparities in predicted bottom-water chemistry across models hampers our ability to robustly estimate the magnitude and temporal evolution of anthropogenic $CaCO_3$ dissolution rates and the associated anthropogenic CO_2 neutralization.

Plain language summary Carbon dioxide (CO_2), produced and released to the atmosphere by human activities, has been accumulating in the oceans for two centuries and will continue to do so well beyond the end of this century if emissions are not curbed. One direct consequence of CO_2 buildup in the ocean is the acidification of seawater. Calcite, a mineral secreted by many organisms living in the surface ocean to produce their shells and skeletons, covers a large part of the seafloor and acts as a natural antacid, neutralizing this excess CO_2. Model projections for the 21st century, under a "business as usual" scenario, reveal that seawater will become more corrosive to this mineral, but calcite dissolution at the seafloor will only increase slightly due to reductions in bottom-current speeds and in the amount of calcite particles delivered to the seafloor over that period. These results indicate that the neutralization of human-made CO_2 by calcite dissolution at the seafloor may take longer than previously anticipated.

1. Introduction

Anthropogenic carbon dioxide (CO_2) has been accumulating in the atmosphere since the beginning of the industrial era and, according to projections of future emissions, will continue to do so well beyond the end of this century (Collins et al., 2013; Meinshausen et al., 2011). The global, mean atmospheric CO_2 concentration was ~280 parts per million (ppm) in 1750 (Joos & Spahni, 2008), reached 405 ppm in 2017 (Dlugokencky & Tans, 2018), and may exceed 1,000 ppm by 2100 according to the "business as usual" Representative Concentration Pathway 8.5 (RCP8.5; van Vuuren et al., 2011), a high-CO_2 emission scenario in which no specific climate mitigation action is taken (Riahi et al., 2011). Each year, about 25% of the

anthropogenic carbon emitted into the atmosphere is absorbed by the ocean (Le Quéré et al., 2018). The absorption of CO_2 in seawater leads to a measurable pH decrease, which, in turn, reduces the carbonate ion (CO_3^{2-}) concentration and lowers the saturation state of seawater with respect to calcium carbonate minerals ($CaCO_3$; e.g., calcite or aragonite), favoring their dissolution and impeding their precipitation (Mackenzie & Andersson, 2013). These conditions are expected to intensify over the next centuries (Boudreau et al., 2010; Boudreau et al., 2018; Caldeira & Wickett, 2003; Orr et al., 2005). Recent research has indicated that the rate of anthropogenic carbon release is higher than during any other comparable event over at least the past 66 million years, highlighting the exceptional nature and rate of ongoing acidification (Zeebe et al., 2016). It is critical that scientists and policy makers obtain accurate estimates of the time scales over which marine ecosystems will be impacted by this anthropogenic ocean acidification.

Two hypothetical pathways can be considered for the evolution of ocean acidification in a high-CO_2 world. In a poorly chemically buffered ocean, CO_2 accumulation and the resulting seawater-pH decline are rapid, leading to runaway ocean acidification. In contrast, a well-buffered ocean can slow down the pH change through negative feedback mechanisms, whose kinetics then control the ocean recovery time toward its pre-acidification state once anthropogenic CO_2 emissions are curbed. One of these feedback mechanisms, the dissolution of marine $CaCO_3$ minerals, is thought to be the major sink for anthropogenic CO_2 on the time scale of decades to millennia (Archer et al., 2009; Ridgwell & Hargreaves, 2007) and is described by the overall reaction:

$$CaCO_3 + CO_2 + H_2O \leftrightarrow 2HCO_3^- + Ca^{2+}. \quad (1)$$

Modern $CaCO_3$-rich sediments (>30% of the sediment dry weight) cover a third of the seafloor (Dutkiewicz et al., 2015; Morse & Mackenzie, 1990). The distribution and $CaCO_3$ content of sediment are a function of the $CaCO_3$ production and export from the surface ocean; dilution of sedimentary $CaCO_3$ by authigenic and siliciclastic materials; and, most importantly, in situ dissolution, which is a function of the saturation state of overlying waters with respect to $CaCO_3$. The latter is defined as

$$\Omega = \frac{[Ca^{2+}]_{SW}[CO_3^{2-}]_{SW}}{K_{sp}^*}, \quad (2)$$

where the square brackets indicate total concentrations in seawater in mol/kg and K_{sp}^* is the stoichiometric solubility constant of the mineral of interest (mol^2/kg^2) at in situ temperature, pressure, and salinity (Millero, 1995; Mucci, 1983). If Ω is lower than 1, seawater is undersaturated with respect to the $CaCO_3$ phase of interest (e.g., calcite or aragonite), which should dissolve if present. Although biogenic aragonite, calcite, and magnesian calcites dominate in the marine environment, only calcite and low magnesian-calcite phases ($MgCO_3$ < 4% by mole) persist in deep-sea sediments (Morse et al., 2007). As ocean acidification intensifies, the area of the seafloor covered by undersaturated waters will increase, and more dissolution of $CaCO_3$ minerals at the seafloor is expected (Alexander et al., 2015; Archer et al., 2009; Boudreau et al., 2010; Ridgwell & Hargreaves, 2007). It is this additional dissolution that neutralizes excess CO_2 and allows projections for the ocean to return to its preacidification state on a multimillennial time scale after anthropogenic emissions are curbed (Boudreau et al., 2018; Ciais et al., 2013).

Currently, 55% of the anthropogenic CO_2 in the ocean is stored in the top 100 m of the water column, while the deep-ocean reservoir (i.e., below ~1,000 m), which represents 76% of the ocean volume, contains only 4% of the anthropogenic CO_2 (from the data of Khatiwala et al., 2009). Through the advection of anthropogenic CO_2-rich surface waters to the deep ocean (see, e.g., MacGilchrist et al., 2019), additional anthropogenic CO_2 will invade the deep sea as CO_2 emissions continue throughout and beyond the 21st century. Whereas most research to date has focused on quantifying anthropogenic CO_2 invasion in the framework of global carbon budget considerations (e.g., Anderson et al., 1998; Khatiwala et al., 2009) or across targeted surface/intermediate waters (e.g., Bates et al., 2012; Carter et al., 2017), the penetration of anthropogenic CO_2 to the abyssal ocean and its impact on pH has not been extensively modeled or monitored. An accurate characterization of bottom-water chemistry and ocean currents is needed to assess the response of

carbonate-rich sediments at the seafloor to anthropogenic acidification. Measurable amounts (i.e., >4 μmol/kg) of anthropogenic CO_2 have been reported in the bottom waters of the Atlantic (Chen, 1982; Körtzinger et al., 1998; Lauvset et al., 2016; McNeil et al., 2003; Perez et al., 2018; Wanninkhof et al., 2013; Woosley et al., 2016), Pacific (Sabine et al., 2002), Arctic (Vázquez-Rodríguez et al., 2009), and Southern (Chen, 1982; Lauvset et al., 2016) Oceans.

In a recent study, Sulpis et al. (2018) showed that anthropogenic bottom-water acidification is now sufficiently advanced to trigger significant sedimentary calcite dissolution in the northwestern Atlantic and the southern extents of the Atlantic, Pacific, and Indian Oceans. Here, we use a diversity of Earth System and climate models to test the premise that over the next century, seafloor calcite dissolution will grow in extent and intensity as acidification persists. To do so, we estimate how global anthropogenic dissolution fluxes at the seafloor will evolve between 2006 and 2100. Subsequently, we test the dependency of benthic dissolution rates to various variables, such as the bottom-water dissolved inorganic carbon concentration and current velocities. Finally, we discuss the need for specific observational constraints to improve relevant model parameterizations.

2. Materials and Methods

2.1. Models and Data

Seawater chemical variables spanning the period 2006 to 2100 were extracted from the RCP8.5 simulations of three different models from the Coupled Model Intercomparison Project Phase 5 (CMIP5): the Global Coupled Climate-Carbon Earth System Model ESM 2M (Dunne, John, et al., 2012; Dunne et al., 2013) developed at the Geophysical Fluid Dynamics Laboratory at Princeton, the IPSL-CM5A Medium Resolution Earth System Model (Dufresne et al., 2013) developed at the Institut Pierre Simon Laplace, and the Hadley Global Environment Model 2 – Carbon Cycle (HadGEM2; Bellouin et al., 2007; Collins et al., 2011) developed at the U.K. Met Office Hadley Centre. Although numerous other CMIP5 models exist, we chose to limit our analysis to these three CMIP5 models for consistency, as they are the only CMIP5 models for which all the bottom-water variables of interest were available. We used annual averages of total alkalinity (*TA*), dissolved inorganic carbon (*DIC*), in situ temperature (*T*), practical salinity (S_P), dissolved inorganic silica concentration ([*dSi*]), soluble reactive phosphate concentration ([*SRP*]), sinking calcite flux (*F*), and seawater (near-)bottom velocity (*U*). The variable [*SRP*] was not available for the HADGEM2C-CC simulation and set at 2 μmol/kg based on Version 2 Global Ocean Data Analysis Project data (Lauvset et al., 2016). All model outputs were horizontally regridded onto the 1° × 1° grid of the World Ocean Atlas. For latitude-longitude coordinate, the deepest layer of the model was considered to be representative of bottom waters. For each model, the bottom-water carbonate ion concentration ($[CO_3^{2-}]_{SW}$) was computed using the MATLAB version of the CO2SYS algorithm (Pierrot et al., 2006; van Heuven et al., 2011), based on bottom-water *TA*, *DIC*, *T*, S_P, [*dSi*], and [*SRP*], using the carbonic acid dissociation constants (K_1^* and K_2^*) from Lueker et al. (2000) and the HSO_4^- dissociation constant from Dickson (1990). We propagated errors in inorganic carbon chemistry according to Orr et al. (2018). In situ temperature and seawater density were computed using the MATLAB version of the GSW Oceanographic Toolbox (McDougall & Barker, 2011).

2.2. $CaCO_3$ Dissolution Rate Calculation

As the salinity of the deep ocean is nearly invariant and the seawater calcium concentration ($[Ca^{2+}]_{SW}$) is practically conservative (i.e., $[Ca^{2+}]_{SW} = f(S_P)$), the saturation state of the deep ocean with respect to calcite, Ω_C, see equation (2), can be represented simply by $[CO_3^{2-}]_{SW}/[CO_3^{2-}]_{eq}$, where $[CO_3^{2-}]_{eq}$ is the seawater carbonate ion concentration at equilibrium with calcite. $[CO_3^{2-}]_{eq}$ was estimated from the equations presented in Boudreau, Middelburg, and Meysman (2010), using $[Ca^{2+}]$ computed from S_P following Riley and Tongudai (1967) and the calcite stoichiometric solubility constant (K_{sp}^*) at in situ *T*, S_P (Mucci, 1983), and pressure (*P*; Millero, 1995).

The depth below which seawater becomes undersaturated with respect to calcite (i.e., $\Omega_C < 1$ or $[CO_3^{2-}]_{SW} < [CO_3^{2-}]_{eq}$) is referred to as the calcite saturation depth (*CSD*). For each model, the *CSD* was computed for each year from 2006 to 2100 using seawater density, $[Ca^{2+}]_{SW}$, $[CO_3^{2-}]_{SW}$, K_{sp}^*, and the equations of Boudreau, Middelburg, and Meysman (2010). Below the *CSD*, seawater is undersaturated with respect to calcite, and dissolution should, according to classical chemical kinetics theory, occur at a rate determined by

the slowest step of the overall reaction (equation (1); Morse & Arvidson, 2002; Naviaux et al., 2019). The slowest step or "kinetic barrier" controlling the rate of calcite dissolution at the seafloor is either the transport of molecular reactants and products across the diffusive boundary layer (DBL; Schlichting, 1979) at the sediment-water interface (typically a few hundred micrometers to a few millimeters thick for deep-sea conditions; Sulpis et al., 2018), or processes within the sediment such as molecular diffusion through the porewaters and reactions at mineral grain surfaces (Boudreau, 2013; Boudreau & Guinasso, 1982; Sulpis et al., 2017). In the first case, the dissolution reaction is termed "water-side transport-controlled" and is strongly dependent on the current speed (U) of the overlying waters (Boudreau & Jørgensen, 2001; Dade, 1993; Steinberger & Hondzo, 1999). Fast bottom currents flatten the DBL and reduce the time necessary for reactants and reaction products to cross the DBL, enhancing the dissolution rate. Conversely, slow bottom-water currents thicken the DBL and impede the dissolution reaction. When processes within the sediment control the dissolution rate, the reaction is termed "sediment-side controlled" and is independent of the overlying water current speed. Currently, calcite dissolution is water-side transport controlled over most of the seafloor but switches to sediment-side control in areas where sediments are calcite poor (Boudreau, 2013; Sulpis et al., 2018). Under this formalism, the dissolution rate is expressed as the product of an overall mass transfer coefficient and a concentration gradient, that is, the deficit in CO_3^{2-} that drives the dissolution reaction.

$$r = k^*\left(\left[CO_3^{2-}\right]_{eq} - \left[CO_3^{2-}\right]_{SW}\right), \tag{3}$$

where k^* is the CO_3^{2-} overall mass transfer coefficient (m/a),

$$k^* = (k_S\beta)(k_S + \beta)^{-1}, \tag{4}$$

where k_s is the sediment-side CO_3^{2-} mass transfer coefficient (m/a) and β is the water-side (DBL) CO_3^{2-} mass transfer coefficient (m/a).

The Calcite Compensation Depth (*CCD*) is the depth at which the calcite dissolution rate at the sediment-water interface equals the sinking flux of calcite delivered to the seafloor, referred to as the rain rate (F; Bramlette, 1961; Edmond, 1974). At steady state (e.g., preindustrial conditions), sediments are calcite-free below the *CCD*. Since the beginning of the industrial revolution, as anthropogenic CO_2 spreads through the deep sea, the oceans are no longer at a steady state, and both the *CCD* and *CSD* have been shoaling (Boudreau, Middelburg, Hofmann, & Meysman, 2010; Feely et al., 2002; Sulpis et al., 2018). As the *CCD* shoals, calcitic particles reaching sediments between the rising *CCD* and the preindustrial *CCD* dissolve completely at the sediment-water interface, but the underlying sediments, although now sitting below the *CCD*, will not become calcite-free for several tens of thousands of years, far beyond the time scale over which this study is focusing (Boudreau & Luo, 2017). Below the preindustrial *CCD*, calcite does not accumulate in sediments because F is compensated entirely by dissolution. Thus, below the preindustrial *CCD*,

$$r = F. \tag{5}$$

For sediments between the preindustrial *CCD* and the rising *CCD*, the net dissolution rate is given by the sum of the carbonate rain rate and the dissolution rate of sediments previously deposited—the sum of equations (3) and (5):

$$r = F + k^*\left(\left[CO_3^{2-}\right]_{eq} - \left[CO_3^{2-}\right]_{SW}\right), \tag{6}$$

where F, k^*, $[CO_3^{2-}]_{eq}$ and $[CO_3^{2-}]_{SW}$ all vary in time. Above the contemporary *CCD*, the rate is computed using equation (3). Here, we use the preindustrial *CCD* values from Sulpis et al. (2018), which are based on measured $CaCO_3$ sediment contents, and initially set the 2006 *CCD* values to the present-day *CCD* values computed by Sulpis et al. (2018). For each CMIP5 model, the *CCD* is subsequently allowed to move freely throughout the 21st century as the simulated seawater chemistry (i.e., $[CO_3^{2-}]_{SW}$), F, and k^* evolve in time according to the equations described in Boudreau, Middelburg, and Meysman (2010). Because the initial *CCD* values were computed from basin-averaged sediment-$CaCO_3$ content profiles (see Sulpis et al., 2018),

CCD predictions are only relevant where the sediment-$CaCO_3$ distribution is controlled by vertical dissolution/deposition fluxes rather than lateral accumulation (i.e., $CaCO_3$ from turbidites or rivers). As the Southern and Arctic Oceans appear to fall in the category of lateral-transport dominated regions, and due to the lack of data in these regions, we exclude the Southern and Arctic Oceans (below 60°S and above 60°N, respectively) and the seafloor shallower than 300 m from our analysis. F, the calcite rain rate, was taken as the deepest simulated sinking calcite flux, expressed in $mol \cdot m^{-2} \cdot a^{-1}$, which we assume to be representative of the calcite flux reaching the seafloor.

β (see equation (4)) was derived from the in situ diffusion coefficient of CO_3^{2-} (Zeebe, 2011), the in situ molecular kinematic viscosity of seawater and bottom speeds (U) for each model, using the equations presented in Sulpis et al. (2018). U was computed as the sum of TPXO9.1 tidal velocities (Egbert & Erofeeva, 2002; downloaded from http://volkov.oce.orst.edu/tides/ and horizontally regridded onto the 1° × 1° grid of the World Ocean Atlas) and annual averages of the resolved horizontal velocities in the deepest layer of each CMIP5 model under the RCP8.5 scenario. Whereas model-resolved velocities change through time, as predicted by each CMIP5 model, TPXO9.1 tidal velocities were assumed constant, given that the effect of climate variability on tidal currents is negligible (Saynisch et al., 2016). U does not include parameterized velocities, such as those arising from the Gent and McWilliams scheme that most models use (see Gent & McWilliams, 1990; Griffies, 1998), because these velocities were not available in the model output. The role of subgrid-scale processes will be discussed in section 4.2. The resulting β distribution is shown in Figure S1 in the supporting information. Since β is dependent on seawater viscosity, it is impacted by variations of seawater T and S_P. β was allowed to evolve as a function of U, T, and S_P between 2006 and 2100, and the impacts of this varying β on the dissolution rates were quantified. k_S, the sediment-side mass transfer coefficient, was computed from the $CaCO_3$ content of the sediments, taken from Sulpis et al. (2018), and set constant throughout the analysis timeframe. The resulting end-of-the-century k_S and the overall mass transfer coefficient, k^*, computed from equation (4), are shown in Figure S1.

2.3. Bottom Currents Across Models

In order to accurately estimate the response of the seafloor to future climate changes, a reliable representation and projection of bottom-current speeds are required. To evaluate the accuracy of the model-predicted bottom-current speeds, the nontidal component of these speeds were compared to a new compilation of current-meter data. The evolution of bottom currents throughout the 21st century was also compared between different coarse resolution models (~1° × ~1°) under RCP8.5 without tides. The current-speed spread between these models is hereafter termed the CMIP5-intermodel spread. In addition, to evaluate the impact of model horizontal resolution on the representation of bottom-current speeds, output of a suite of three climate models of different resolution (the CM2-O suite) were compared. The CM2-O suite includes CM2.6 (Griffies et al., 2015; Winton et al., 2014), which uses a (1/10)° horizontal resolution, CM2.5 (Delworth et al., 2012), with a (1/4)° horizontal resolution, and CM2-1deg (Griffies et al., 2015), with a 1° horizontal resolution. The CM2-O models were run under an atmospheric partial pressure of CO_2 (pCO_2) increase of 1%/year for 70 years starting at 286 ppm. This idealized CO_2 concentration scenario is similar to the RCP8.5 scenario used in the three CMIP5 models investigated in this study. Finally, we also used four simulations from the HYbrid Coordinate Ocean Model (HYCOM; Trossman et al., 2016; an ocean-sea ice model forced with atmospheric reanalyses—note that these simulations are of the present-day ocean only). Two of the HYCOM simulations were run in a (1/12)° configuration, and two were run in a (1/25)° configuration, with each configuration comprising one simulation that included a parameterized topographic internal lee wave drag, and another simulation without it, as described in Trossman et al. (2016). Here, "wave drag" refers to the momentum sink associated with the generation of internal lee waves and accounts for a breaking effect when the geostrophic flow impinges upon rough topography, based on the theory of Garner (2005) and applied in Trossman et al. (2013). Analogous to the CMIP5 models, neither the CM2-O models nor HYCOM currently include tides.

The current-meter data set contains measurements described by Trossman et al. (2016) and Luecke et al. (2017). In order to remove tidal currents from the measurements, a low-pass filter was applied to each current-meter record. Only records containing a minimum of 105 days of observations were considered, following Timko et al. (2013). At each location, measurements within 500 m of the seafloor were averaged and considered to be representative of bottom currents, for comparison with bottom-current values simulated by

models. We chose to average current-meter measurements over the bottom 500 m because these values are close to the vertical resolution in the deepest layers of the models, where the current speed comparison takes place. There is a trade-off between the decreasing number of observations available as we get closer to the seafloor and the representativeness of the current speeds farther from the seafloor. An upper boundary at 500 m above the seafloor allows us to resolve an entire model layer, as well as having a reasonably large number of current-meter observations. Using only data at locations where at least two instruments were available within the bottom 500 m, with seafloor depths exceeding 1,000 m, our current-meter data set comprises measured current speeds over 378 locations.

3. Results

3.1. Modeled Changes in Bottom-Water Properties Under the RCP8.5 Scenario

According to the CMIP5 model mean temperature predictions throughout this century, an important warming of bottom waters occurs near the continents, where the seafloor is shallow, and in the Southern Ocean, as shown in Figure 1a and in Purkey and Johnson (2010). Conversely, the bottom-water temperatures in the northwestern Atlantic display a sharp cooling of ~0.6 °C by the end of this century, in agreement with the current abyssal cooling trend in this basin (Desbruyères et al., 2016). This is likely attributable to the decline in the meridional overturning circulation strength because the overturning cell becomes shallower and less heat is transported from the surface to the abyss (Caesar et al., 2018; Rhein et al., 2011; Thornalley et al., 2018; Zhang, 2008). Globally, under the RCP8.5 scenario, mean bottom-water temperatures are projected to increase by ~0.2 °C between the first and the last 30 years of this century. Concomitantly, an important freshening of bottom waters is projected in high boreal latitudes, while bottom waters in the Southern Ocean become saltier (Figure 1b), in line with the results of Heuzé et al. (2015) and Meijers (2014). In contrast, recent studies have reported freshening of Antarctic Bottom Waters (AABW), based on hydrographic data, that is thought to be caused by glacial melting (Menezes et al., 2017; Purkey & Johnson, 2013). Warmer and saltier AABW would be consistent with reduced ventilation in this area (de Lavergne et al., 2014), as predicted by ESM 2M (Figure S2), as weakening deep convection around Antarctica brings less, relatively cold and fresher waters to the bottom. Coarse resolution climate models, such as the CMIP5 models used here, generally form AABW by open-ocean convection, something that is thought to rarely happen in nature. Only very fine resolution (greater than 0.1°) models are able to form some AABW from dense water generated on the shelf cascading to the abyss (e.g. Bryan et al., 2014; Dufour et al., 2017; Newsom et al., 2016).

Global bottom-water *DIC* rises by an average of 9 μmol/kg, a 0.4% increase relative to the beginning of the century (Figure 1c). Some of the largest bottom-water *DIC* increases are projected to occur in the northern Atlantic where the bottom waters are youngest (Huiskamp & Meissner, 2012; Matsumoto, 2007) and rich in anthropogenic CO_2. In the Labrador Sea and at the southern edge of Greenland, the *DIC* increases are as high as +70 μmol/kg, a ~3% increase relative to the beginning of the century. We also note an acute increase (+~40 μmol/kg) of *DIC* along the western fringe of the Atlantic and Pacific Oceans. A weaker but more spatially extended *DIC* increase of ~10 μmol/kg in the southern half of the globe is also predicted, which can be attributed partly to the northward spreading of the dense and young AABW (de Lavergne et al., 2017; Gebbie & Huybers, 2012). The elongated positive *DIC* anomaly in the low latitudes of the Pacific Ocean (i.e., between Peru and Melanesia) is driven by an accumulation of metabolic CO_2, as an increase in both the age of bottom waters (see Figure S2) and the particulate organic carbon sinking flux (see Figure S3) is predicted in this area. Older bottom waters may reflect weakened bottom currents (see section 4.2) and/or reduced bottom-water mixing. Older bottom waters accumulate more metabolic products (nutrients, *DIC*) resulting from the oxic catabolism of sinking organic material, explaining the positive anomaly in *DIC*, [*SRP*], and [*dSi*] in the equatorial Pacific, Southern Ocean, and Northern Atlantic.

Under the RCP8.5 scenario, the global mean bottom-water *TA* is stable, increasing by only ~0.5 μmol/kg during the 21st century (Figure 1d). Potential sources for *TA* include $CaCO_3$ dissolution and the addition of nutrients (*SRP* or *dSi*) to seawater. In fact, bottom-water *SRP* (Figure 1e) and *dSi* (Figure 1f) concentrations strongly increase in the Atlantic Ocean, while they decrease in the Arctic Ocean, as seen in Figures 1e and 1f, and the relative changes in *TA*, *SRP*, and *dSi* are highly correlated in most of the bottom waters, as shown in Figure S4.

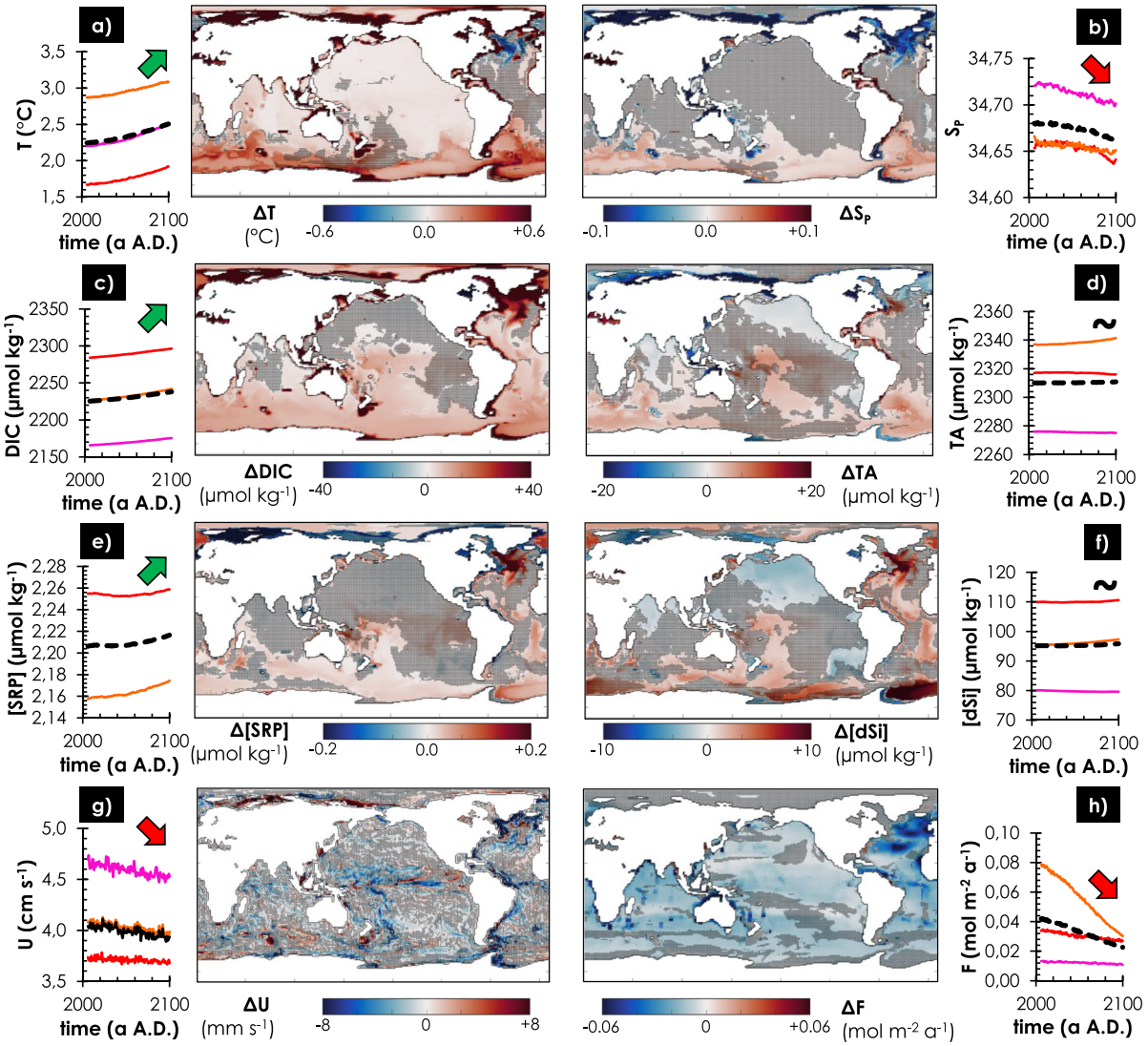

Figure 1. Changes (Δ) in bottom-water (a) temperature (Δ*T*), (b) practical salinity (ΔS_P), (c) dissolved inorganic carbon concentration (Δ*DIC*), (d) total alkalinity (Δ*TA*), (e) soluble reactive phosphate concentration (Δ[*SRP*]), (f) dissolved inorganic silica concentration (Δ[*dSi*]), (g) bottom-current speed (Δ*U*), and (h) calcite flux to the seafloor (Δ*F*) between the first 30 years (2006–2035) and the last 30 years (2071–2100) of the CMIP5 model mean, under the RCP8.5 scenario. Each map is associated with an adjacent plot that shows the annual mean of the globally averaged variables for the CMIP5 model mean (black dashed line), ESM 2M (orange line), HadGEM2 (pink line), and IPSL (red line) between 2006 and 2100. Qualitative results from Mann-Kendall trend tests (Kendall, 1975; Mann, 1945) performed on the globally averaged CMIP5 model mean values between 2006 and 2100 are also shown. This test identifies whether there is a consistently increasing or decreasing monotonic trend. The sign of the trend for each variable is depicted with green arrows for statistically significant increasing trends, red arrows for statistically significant decreasing trends, and tilde symbols for diverging trends. Statistics associated with each trend test are reported in Table S1. Gray-shaded regions are areas where models disagree regarding the sign of the trend.

The modeled changes in *U* are spatially highly heterogeneous (Figure 1g) making it challenging to identify coherent regional modifications. Nevertheless, in a warm, high-CO_2 world, the CMIP5 model mean *U* globally declines by ~2% (between 1% and 3%, depending on the model) by the end of the century. Bottom currents weaken notably near the equator and Northern Atlantic, and by up to 40% by the end of the century offshore of Newfoundland.

Finally, the downward flux of calcite reaching the seafloor, *F*, is predicted to show a ubiquitous decline (Figure 1h). The CMIP5 model mean *F* decreases by 25% (between 11% and 48%, depending on the model) by the end of the 21st century. We attribute this abated *F* to reduced surface production and export, and increased water-column $CaCO_3$ dissolution. Although the magnitude of *F* decline is greater at low latitudes where the $CaCO_3$ rain rate is highest, the relative *F* decline is greater and more important at high latitudes.

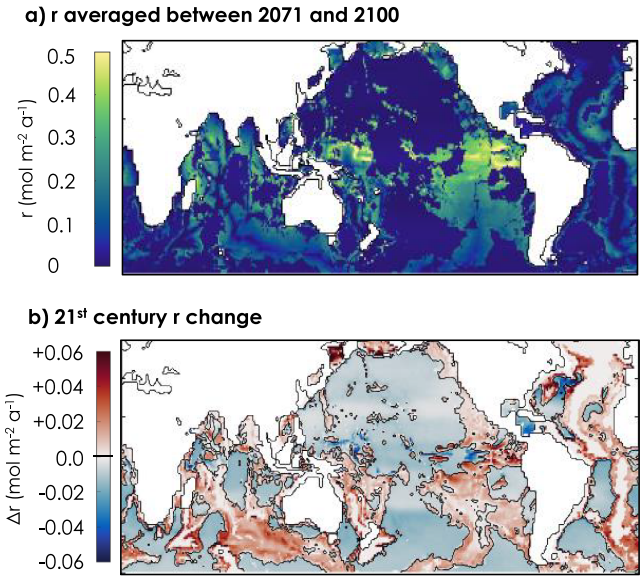

Figure 2. CMIP5 model mean (a) calcite dissolution rate (r) at the sediment-water interface averaged between 2071 and 2100 and (b) change in the dissolution rate (Δr) between the first 30 years and the last 30 years of the 21st century.

By the end of this century (i.e., average 2071–2100) and outside of the high latitudes, the CMIP5 model mean *CSD* will be 2,041 m, which is 146 m shallower than the 2006–2035 average value. In comparison, Sulpis et al. (2018) computed a *CSD* rise of 142 m between the end of the preindustrial period (i.e., 1800) and 2002. These results suggest that the *CSD* rise is accelerating as we go further into the Anthropocene.

3.2. Calcite Dissolution Rate

At the end of the 21st century, the fastest benthic $CaCO_3$ dissolution (r) will occur in the equatorial Pacific (Figure 2a), where bottom waters are strongly undersaturated with respect to calcite, sediments are rich in $CaCO_3$, and bottom currents are fast (see Figure S1). Areas located between the preindustrial and the rising *CCD*, which corresponds to topographic highs, are associated with important dissolution rate increases, while the deeper areas of the ocean, located below the preindustrial *CCD*, show a dissolution rate decrease. In the eastern equatorial Pacific, meridional shifts in bottom currents will cause abrupt changes in the benthic dissolution rates. In the northern half of the central Pacific, between the Fiji Plateau and the Aleutian Trench, a large area of reduced r will develop, explained primarily by a drop in F (Figure 3b). In this area, except for the Hawaiian archipelago, the seafloor is located below the *CCD*. Thus, the calcite dissolution rate at the seafloor is constrained by the calcite rain rate, according to equation (5), regardless of any DBL limitation and, thus, independent of bottom currents. The same is true for the southern extents of the Atlantic, Pacific, and Indian Oceans, where most of the seafloor is below the *CCD* and seafloor dissolution depends only on rain rate changes. Although a large amount of anthropogenic CO_2 enters the deep ocean in the North Atlantic, this CO_2 does not spread into the deepest layers of the abyssal Atlantic (see Figure 1). In fact, most of the seafloor in this basin is covered by colder and denser AABW (Johnson, 2008; Morozov et al., 2010), nearly devoid of anthropogenic CO_2 except for its most southern extent (Ríos et al., 2015), as it takes several centuries for the AABW to reach the Equator in the Atlantic Ocean basin (Huiskamp & Meissner, 2012).

By isolating the effect of each controlling variable on the overall benthic dissolution rate (Figure 3a), we reveal that while increasing bottom-water *DIC* globally drives the dissolution rate up during the 21st century, bottom-water total alkalinity (*TA*), bottom-current speeds (U), and calcite rain rates (F) lower the dissolution rate. A reduction in the calcite flux reaching the deep ocean (F) leads to a lower dissolution rate below the *CCD*, according to equations (5) and (6), and causes the *CCD* to rise much faster (Boudreau, Middelburg, & Meysman, 2010). We estimate that the CMIP5 model mean world-averaged *CCD* will rise from 4,465 ± 378 m at the beginning of the 21st century to 3,677 ± 715 m by the end of the century—a

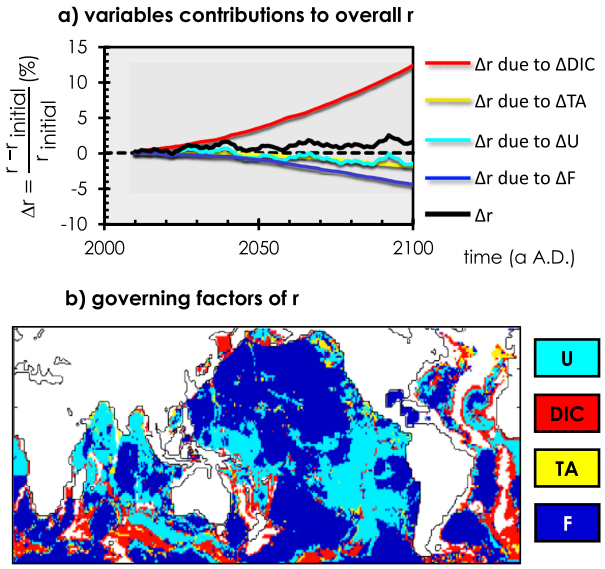

Figure 3. (a) CMIP5 model mean temporal evolution of the global-averaged benthic dissolution rate anomaly relative to 2006 (Δr) and the respective contributions of *U* (light blue), *DIC* (red), *TA* (yellow), and *F* (dark blue) to the dissolution rate anomaly. Respective contributions of each variable were estimated by computing the dissolution rate through time when all variables are kept constant throughout the 21st century, except for the variable whose contribution is to be quantified. (b) Geographical distribution of the primary driver of the benthic dissolution rate, variables with the highest correlation coefficient (R^2) resulting from a multiple multivariate linear regression of *r* against *U*, *DIC*, *TA*, and *F*.

788 ± 809 m shoaling in less than a century. Whereas 83 to 168 × 10^6 km^2 (28% to 57%) of the seafloor are located below the *CCD* at the beginning of the century (outside of high latitudes), this area grows to between 130 and 243 × 10^6 km^2 (45% to 83%) by the end of the century. In other words, due to the predicted *CCD* rise, 61 ± 70 × 10^6 km^2 (21 ± 24%) of the seafloor could switch from being the locus of net $CaCO_3$ accumulation to net dissolution. Changes in *F* dominate the 21st century benthic dissolution rate variations over most of the high latitudes and deep abyssal plains, as the seafloor in these areas resides, for the most part, below the *CCD*. *DIC*- and *TA*-driven dissolution rate changes are more important in shallower areas, corresponding to topographic highs or coastal areas, as shown in Figure 3b. Finally, the global decrease in bottom-current speeds increases the average DBL thickness and leads to a small but widespread slowdown of the calcite dissolution rate at the seafloor. Dissolution rate reduction due to bottom-current changes is important at low latitudes, and over the mid-ocean Indian and Pacific ridges (Figure 3b). Globally, throughout the 21st century and under RCP8.5, the calcite rain rate (*F*) and bottom-current speed (*U*) govern the seafloor calcite dissolution rate changes over 53% and 31% of the dissolving seafloor (i.e., the area of the seafloor overlain by undersaturated bottom waters), respectively. Other factors, such as *DIC* and *TA*, dominate the calcite dissolution changes over much smaller portions of the seafloor (13% and 3%, respectively). Variations of bottom-water *T*, S_P, [*SRP*], and [*dSi*] do not exert a strong influence on the benthic dissolution rate, as each impact the rate by less than 1% throughout the 21st century.

4. Discussion

4.1. Formulating Calcite Dissolution in Sediments

The novelty of the present approach rests with the inclusion of the effects of both bottom-water chemistry and current velocity information on dissolution rates. Doing so, we are able to identify areas of focused dissolution where high bottom-water velocities are prevalent as well as areas where climate warming reduces such velocities and associated dissolution. Nevertheless, our dissolution rate model does not include oxic or anoxic respiration-driven dissolution. In Figure 4, we provide a comparison of our 2006–2035 dissolution rates with those obtained by Dunne, Hales, and Toggweiler (2012). The model developed by Dunne, Hales, and Toggweiler (2012) accounts for organic matter respiration within the oxic zone of the

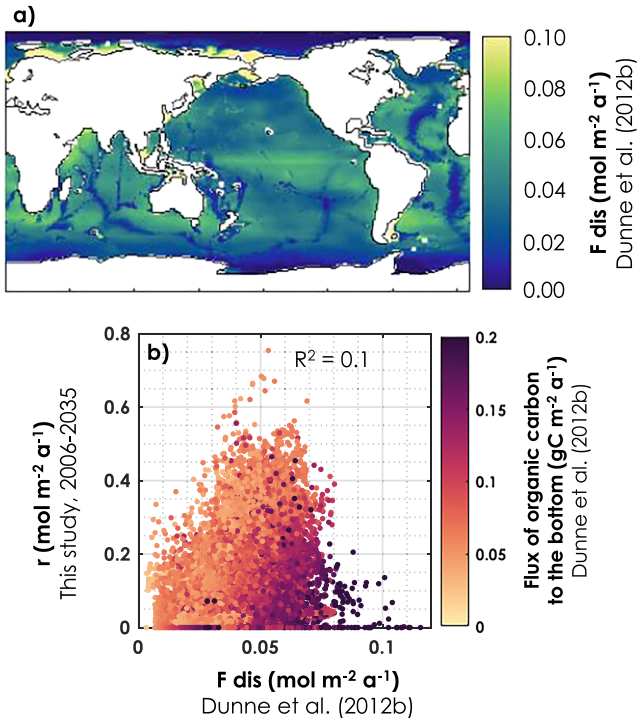

Figure 4. (a) Dissolution rates from Dunne, Hales, and Toggweiler (2012), which we term F_{dis}. The F_{dis} values from Dunne, Hales, and Toggweiler (2012) were computed by subtracting their final modeled calcite burial flux from their final modelled calcite bottom flux. Hence, F_{dis} does not necessarily represents the dissolution rate of calcite at the sediment-water interface, but rather the fraction of the calcite flux to the bottom that is being dissolved either at the sediment-water interface or within the sediment porewaters. (b) Scatter plot that compares r values from this study with F_{dis} values from Dunne, Hales, and Toggweiler (2012). The flux of organic carbon to the bottom is taken from Dunne, Hales, and Toggweiler (2012). The correlation coefficient (R^2) describing the agreement between r and F_{dis} values is also shown.

sediments, and metabolic CO_2 production, which can locally reduce the porewater calcite saturation state and trigger dissolution regardless of the overlying water column chemistry (Archer, 1996; Hales, 2003; Mekik et al., 2002). As our computations do not consider metabolic dissolution, our model underestimates dissolution rates relative to those derived by Dunne, Hales, and Toggweiler (2012) in areas of high organic carbon fluxes at the seafloor (Figure 5d). In these areas, future changes in organic carbon fluxes to the seafloor (e.g., see Figure S3) could affect calcite dissolution in sediments.

Likewise, other factors such as changes in bottom-water temperatures or dissolved oxygen concentrations could influence the activity of burrowing organisms, enhancing or impeding bioirrigation or bioturbation, processes that can locally modify porewater solute distributions and fluxes across the sediment-water interface (Boudreau & Jørgensen, 2001; Meysman et al., 2006; Teal et al., 2008). Regrettably, in the absence of observations of changes in deep-sea burrowing organism activity and/or in benthic organic carbon fluxes, we cannot expand on this further.

On the other hand, the model of Dunne, Hales, and Toggweiler (2012) does not take into consideration the presence of a current-speed dependent DBL above the sediment-water interface. Most sediment models published to date either ignore the presence of a DBL above the sediment-water interface or consider a DBL with a thickness set to a constant arbitrary value (Archer et al., 2002; Boudreau, 1996; Hales, 2003; Heinze et al., 1999; Munhoven, 2007; Tschumi et al., 2011; van Cappellen & Wang, 1996). Instead, the DBL thickness should be expressed as a function of current speed, as formulated by various authors (Boudreau & Guinasso, 1982; Higashino & Stefan, 2004; Levich, 1962; Sulpis et al., 2018) and confirmed by experimentalists (Larkum et al., 2003; Lorke et al., 2003; Santschi et al., 1983; Santschi et al., 1991). As shown in Figure 4, the present study, which uses a current-speed dependent DBL thickness, predicts dissolution rates that are higher than those derived by Dunne, Hales, and Toggweiler (2012) in areas of fast bottom currents. Future

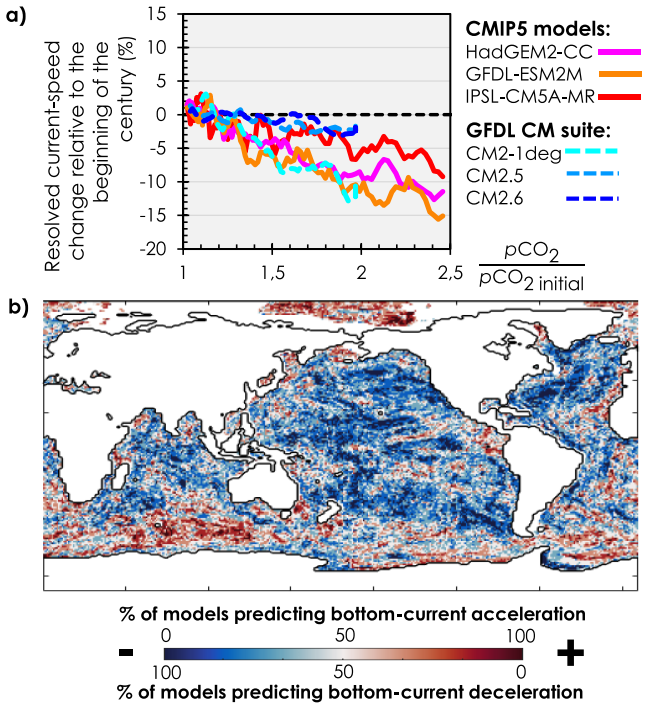

Figure 5. Intercomparison of the resolved bottom-current speed response of six Earth System and climate models to atmospheric pCO_2 accumulation. (a) World-averaged, resolved bottom-current speed changes relative to the beginning of the simulation, as a function of relative change to atmospheric pCO_2 for bottom waters deeper than 1 km and between 60°S and 60°N. $pCO_{2\ initial}$ is the world-averaged atmospheric pCO_2 for the first year of each simulation. pCO_2 values for the models under the RCP8.5 scenario are taken from Meinshausen et al. (2011). The solid lines represent running averages over a 5-year period. Mann-Kendall trend test (Kendall, 1975; Mann, 1945) results for each of the model output are shown in Table S2. The dashed black line indicates the baseline. (b) Sign of the bottom-current speed change between the first and the last 30 years of the six simulations. The dark blue end of the color spectrum represents a case where all six models predict a bottom-current speed decrease, whereas the dark red end indicates the case where all six models predict a bottom-current speed increase.

research efforts should focus on developing sediment modules inclusive of both sedimentary organic carbon degradation and mass transfer through a DBL of variable thickness.

According to our calculations, 25.3 ± 16.0 Tmol of $CaCO_3$ dissolves each year at the sediment-water interface at the beginning of the 21st century. In contrast, using the data of Dunne, Hales, and Toggweiler (2012), we estimate that only 13 Tmol of $CaCO_3$ is dissolved each year within marine sediments. These values represent only 20.7% and 10.6%, respectively, of the total pelagic $CaCO_3$ dissolution estimated by Smith and Mackenzie (2016). In comparison, Berelson et al. (2007) and Sulpis et al. (2018) estimated the modern seafloor calcite dissolution flux at 33 ± 25 and 32 ± 12 Tmol/a, respectively. The low dissolution rates that we find compared to observational estimates could result from an overestimate of the DBL thickness. Based on CMIP5 bottom-current speeds, to which tidal current speeds were added (see section 2), the CMIP5 model mean DBL thickness is estimated at ~1.8 mm. According to observations, this value can be reached in the deep sea but may be too thick for a global mean value, generally thought to be thinner, from 200 μm to 1 mm thick (Boudreau & Jørgensen, 2001; Santschi et al., 1991; Sulpis et al., 2018). The overestimated DBL thickness in models likely results from an underestimate of the bottom-current speeds simulated by models (e.g., velocities arising from mesoscale and submesoscale processes). Overestimating the DBL thickness in a model where the dissolution is limited by diffusion through the DBL, such as ours, underestimates the true dissolution rate and may explain the discrepancy in the global $CaCO_3$ dissolution magnitude identified above. In the following discussion, we investigate the bottom-current representation in models.

4.2. Modeled Bottom Currents

Under increasing atmospheric pCO_2, all models tested here predict a bottom-current speed decrease (Figure 5), and these decreasing trends are statistically significant (Figure 5 and Table S2). On average,

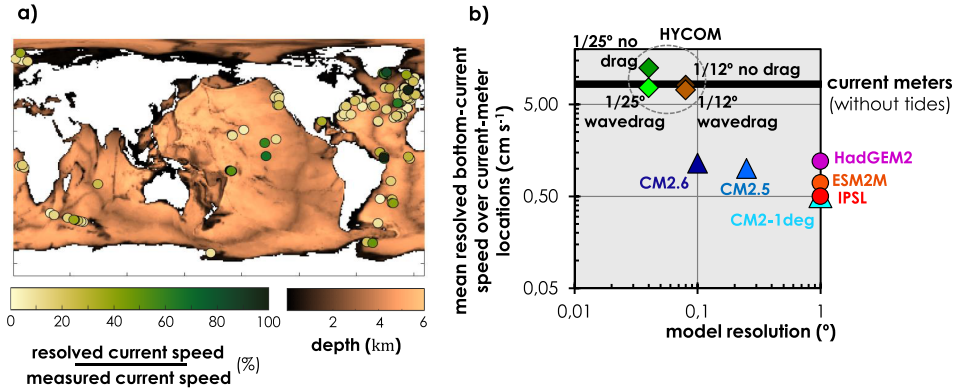

Figure 6. Comparison of the resolved bottom-current speeds between models and observations. (a) Ratio of the collocated current speed from the CMIP5 model mean to current-meter observations. (b) Bottom-current speeds averaged over 378 current-meter locations deeper than 1 km in the three CMIP5 models, three CM2-O models, and four configurations of the HYCOM model (see section 5.2 for description of the models) as a function of the model resolution. The black, thick line represents the current-meter average. For simplicity, the CMIP5 models are considered to be of 1° × 1° resolution.

the six models predicted the world-averaged, resolved current speed to drop by 6.8 ± 3.9% upon doubling of the preindustrial atmospheric pCO_2. As shown in Figure 5b, all models predict a bottom-current slowdown in several areas of the North Atlantic, the Equatorial Atlantic, and most of the Pacific Ocean, consistent with the results of Cheng et al. (2013). This slowdown is likely linked to a weakening of the Atlantic meridional overturning circulation and a reduced ventilation in the North Atlantic (Caesar et al., 2018; Pérez et al., 2013; Steinfeldt et al., 2009; Thornalley et al., 2018; Wanninkhof et al., 2010; Zhang, 2008). Collins et al. (2013) estimated that the strength of the Atlantic meridional overturning circulation will drop by 12–54% during the 21st century under RCP8.5. Likewise, in the Southern Ocean, anthropogenic surface-water freshening may cause a weakening in the production of AABW (de Lavergne et al., 2014).

Although the trend of decreasing bottom-current over this century is a consistent feature across CMIP5 and CM2-O models, a comparison of these modeled bottom velocities with current-meter observations shows that below 1-km depth, where most calcite dissolution occurs, these models consistently underestimate bottom-current speeds (Figure 6). Because neither the models used in this study nor our current-meter data set include tides, these discrepancies are due to a lack of resolved motions and physics, not to a lack of tidal velocities in models. Only the HYCOM simulations successfully reproduce the magnitude of observed bottom-current speeds (Figure 6). Nevertheless, the correlation coefficient of the modeled, resolved current speeds to the measurements for the HYCOM simulations are lower than those for the CMIP5 and CM2-O models (Figure 7). The correlations between output of the higher resolution models and the current meter observations are not expected to be as strong as those of the coarser resolution models because of the difficulty of colocating currents at high resolution. In fact, the correlation coefficients between the outputs of higher-resolution models and the currentmeter observations increase when the higher-resolution model outputs are smoothed onto the same grid as the coarser resolution models.

Mesoscale eddies carry a large proportion of the flow from the surface to the bottom and are only resolved for ocean models with horizontal resolutions higher than about (1/5)° at ~30°N or S, (1/10)° at ~60°N or S (Hallberg, 2013; Hecht & Hasumi, 2008). Thus, the three CMIP5 models used in this study have a horizontal resolution that is too coarse to explicitly resolve these eddies. Instead, these models rely on a mesoscale eddy transport parameterization (see Gent & McWilliams, 1990; Griffies, 1998). In addition, the use of geopotential-height vertical coordinates requires additional schemes to accurately represent bottom-following flows (e.g., Adcroft et al., 1997) and can result in their misrepresentation (Dunne, John, et al., 2012). In Figure S5, we show that, in CM2-1deg, the parameterized bottom-current speeds associated with the mesoscale are generally less than 5% of the resolved current speeds, except at high latitudes. Similarly, using the Marshall and Adcroft (2010) mesoscale eddy kinetic energy framework, Melet et al. (2015) showed that the resolved bottom velocities are generally higher than the parameterized bottom mesoscale velocities. According to Melet et al. (2015), the contribution of the parameterized bottom speed to the total bottom

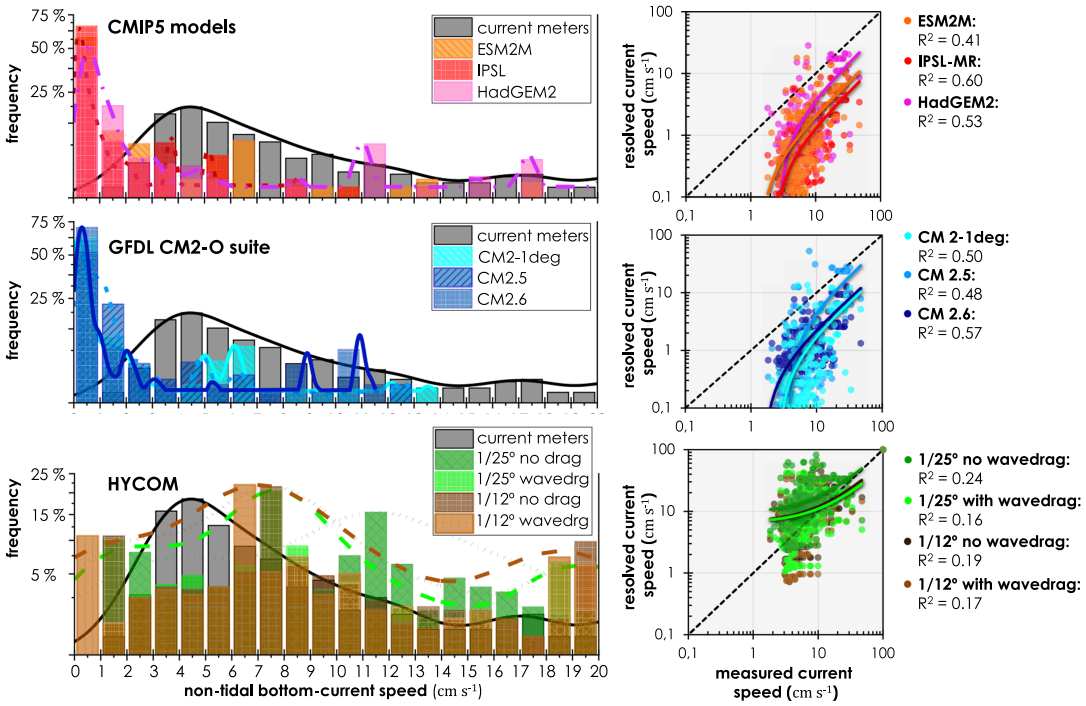

Figure 7. (Left column) Histograms of the distribution of resolved bottom-current speeds corresponding to the 378 current-meter sites deeper than 1 km. Lines represent kernel density functions. (Right column) Correlation diagrams between measured bottom-current speeds and model-simulated values. Both the current-meter measurements and model predictions do not include tides. Correlation coefficients (R^2) are shown for each model.

speed is of generally 1/3 (Angélique Melet, personal communication) although it is larger in the Southern Ocean; see Figure 3 in Melet et al. (2015). Thus, it is unlikely that the unresolved, parameterized flows account for the order of magnitude discrepancy between the coarse resolution models and the current-speed observations. Pearson et al. (2017) found that reduced water viscosity in models leads to stronger bottom currents. The bottom-current speed underestimation by CM2.6 is surprising, given its relatively high resolution, and we speculate, based upon the Pearson et al. (2017) results, that the differences between CM2.6 and the HYCOM simulations might be due to different viscosity coefficients (see, e.g., Griffies & Hallberg, 2000, and Wallcraft et al., 2005), or methods of applying bottom-drag. We also note that as model resolution is refined in the CM2-O suite, the globally averaged bottom currents are faster (Figure 6b). Finally, in regions of rough topography and strong bottom currents, submesoscale instabilities might generate currents with velocities that exceed those resolved by models (e.g., Callies, 2018), which could explain some of the discrepancies highlighted here.

In brief, our results of 21st-century dissolution changes being dominated by $CaCO_3$ sinking flux variations rely on several assumptions regarding future bottom currents, all of which could be verified by future research: First, tidal velocities will not be impacted by climate change; second, barotropic tidal velocities dominate over baroclinic tidal velocities near the seafloor; third, CMIP5 models accurately predict the trend in the resolved velocities near the seafloor; and fourth, the trend in the (sub)mesoscale velocities near the seafloor is dominated by the trend in resolved velocities. Notwithstanding, given that mesoscale velocities near the seafloor are also projected to decrease through the 21st century due to anthropogenic CO_2 emissions (Melet et al., 2015), the overall bottom speeds—and associated dissolution rate—decrease could be larger than what is reported here.

4.3. Global $CaCO_3$ Dissolution and Sources of Uncertainty

Our results show that $CaCO_3$ dissolution at the seafloor will be delayed by the combination of an abated biogenic $CaCO_3$ delivery to the seafloor, bottom-current slowdown, and alkalinization of bottom waters. Nevertheless, model disagreements reveal large uncertainties regarding the role of controlling variables,

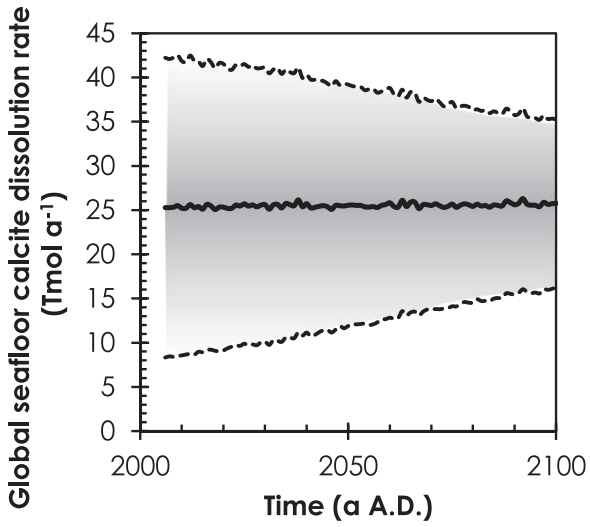

Figure 8. Global seafloor calcite dissolution rate as a function of time, simulated by the CMIP5 model mean under the RCP8.5 scenario (black line), accounting for the uncertainties associated with each CMIP5 model mean variable (CMIP5-intermodel spread) and their propagation into the computed dissolution rates (gray-shaded area).

thus preventing the accurate prediction of $CaCO_3$ cycling at the seafloor over the next century. Figure 8 represents the global 21st century calcite dissolution rate, computed from the CMIP5 model variables using the sum of the TPXO9.1 tidal velocities and the bottom velocities as resolved by the models. The standard deviation was computed using standard error propagation rules following Sulpis et al. (2018). Despite large cumulative errors that hinder accurate future calcite dissolution predictions, a Mann-Kendall trend test reveals that the global seafloor calcite dissolution rate evolves during the 21st century under RCP8.5 with a statistically significant increasing trend ($p = 2 \times 10^{-5}$).

The uncertainty associated with the computed $[CO_3^{2-}]_{SW}$ was derived using the code from Orr et al. (2018). In year 2100, the scaled-up seafloor calcite dissolution rate is 25.6 ± 10.6 Tmol/a, statistically indistinguishable from the 2006–2035 averaged rate of 25.3 ± 16.0 Tmol/a, due to the wide error bars. As can be seen in Figure 1, the modeled values of many bottom-water variables are different depending on the model. From the three CMIP5 models used in this study, the world-averaged intermodel standard deviations for *TA* and *DIC* are 40 and 66 μmol/kg, respectively, which represents more than 10 times the usual measurement errors (Millero, 2007; Olsen et al., 2016). The computed bottom-water CO_3^{2-} concentration is, thus, highly dependent on the model, which inhibits our ability to accurately simulate dissolution rates in the present or future.

Given that the delivery of biogenic $CaCO_3$ to the seafloor is the primary control on benthic $CaCO_3$ dissolution throughout the 21st century and that the spread in CMIP5 predictions of $CaCO_3$ rain rate is very large, most of the uncertainty in our dissolution rate predictions originates from the $CaCO_3$ rain rate uncertainty. In fact, the standard deviation across models on the world-averaged calcite flux to the bottom is larger than its mean value throughout the entire century. Whether at the surface ocean or at depth, our inability to precisely quantify the $CaCO_3$ rain rate has already been pointed out by Berelson et al. (2007). Similarly, experimental investigations of the response of $CaCO_3$ surface production to elevated CO_2 conditions have reported disparate responses (Fukuda et al., 2014; Maugendre et al., 2017; Pinsonneault et al., 2012; Wootton et al., 2008). In the next century, while coccolithophores could initially benefit from elevated CO_2 concentrations, global calcification could ultimately be reduced relative to the end of the preindustrial era, under end-of-the-century RCP8.5 atmospheric CO_2 levels (Krumhardt et al., 2019). Direct suppression of biogenic $CaCO_3$ production under seawater acidification is absent from many models or otherwise often highly parameterized and probably overly deterministic. There are ongoing debates about what actually drives calcification, which consequently should represent a priority for both experimental and modeling work (see Fassbender et al., 2016, and references therein). According to results presented here, an accurate representation of the biogenic $CaCO_3$ export and rain rate in Earth System and climate models should be a priority for future

model developments. This recommendation is in line with the conclusion reached by Boudreau et al. (2018) on the role of a changing carbonate rain/calcification rate in enhancing or reducing $CaCO_3$ preservation over longer time scales. Independent modeling approaches suggest that the calcification rate is a central player in acidification dynamics.

5. Conclusion

Calcite dissolution rates at the seafloor are controlled by a variety of processes that will evolve under projected warming and acidification. Whereas ocean acidification controls the thermodynamic potential of the dissolution reaction, widening the gap between $[CO_3^{2-}]_{SW}$ and $[CO_3^{2-}]_{eq}$, and driving calcite toward dissolution, the dissolution rate at the seafloor also depends on kinetic processes that are independent of solution chemistry, such as the resistance caused by the presence of a DBL above the seafloor, whose thickness is dependent on bottom-current speeds that are also projected to change. Traditionally, the balance of $CaCO_3$ fluxes at the sediment-water interface has been expected to shift toward enhanced dissolution in response to any acidification event (Archer et al., 1998; Boudreau, 2013; Broecker & Peng, 1982; Eyre et al., 2018; Sulpis et al., 2018). Our results show that within the 21st century, when various processes affecting the calcite dissolution rate at the seafloor are considered, the dissolution rate increase is lower that what would be predicted when considering bottom-water acidification only, due to a combination of both a decreasing supply of calcite from above and bottom-current velocity. The general slowdown of bottom currents and declining $CaCO_3$ flux to the seafloor counteract the effect of ocean acidification on the calcite dissolution rate at the seafloor. One should, however, be wary of simply extrapolating such results over longer time scales.

Over more than half of the dissolving seafloor, benthic $CaCO_3$ dissolution rate changes through the 21st century will be primarily driven by declining $CaCO_3$ rain rates. Thus, a better representation of $CaCO_3$ settling fluxes, as well as the $CaCO_3$ production response to elevated CO_2 concentrations, should be a priority for future model developments. Even though most recent models strongly underestimate modern bottom-current speeds relative to field observations, partly due to the low-resolution of the ocean component, all models tested in this study consistently predict a global decrease in the strength of bottom circulation. To accurately represent the magnitude and loci of calcite dissolution at the seafloor, models must better represent bottom-water chemistry, bottom currents, and integrate a DBL module in which the DBL thickness fluctuates according to the hydrodynamics at the seafloor. This work suggests that seafloor calcite dissolution in response to the ongoing acidification event and its associated CO_2 sink may be delayed and has important implications in our understanding of calcite dissolution and preservation and CO_2 neutralization on geological time scales.

Acknowledgments
The authors declare no conflict of interest. We thank Angélique Melet and Richard E. Thomson for fruitful discussions, as well as Lori Sentman, Robbie Toggweiler, and two anonymous reviewers for helpful comments and suggestions. We acknowledge the World Climate Research Programme's Working Group on Coupled Modelling, which is responsible for CMIP, and we thank the individual climate modeling groups for producing and making available their model output. The U.S. Department of Energy's Program for Climate Model Diagnosis and Intercomparison provides coordinating support and led development of the For CMIP software infrastructure in partnership with the Global Organization for Earth System Science Portals. We thank the Geophysical Fluid Dynamics Group (GFDL) at Princeton for sharing the model output of the CM2-O suite. D. S. T. and B. K. A. thank their coauthors in Trossman et al. (2016) for allowing them to access the HYCOM results used in this paper. Grants of computer time were provided by the Department of Defense (DoD) High Performance Computing Modernization Program and by the National Center for Atmospheric Research (NCAR) Yellowstone university allocations. D. S. T. and B. K. A. thank Rob Scott who compiled the original current meter database that we have modified for use in their papers including this one. O. S. acknowledges the Department of Earth and Planetary Sciences at McGill University and the Natural Sciences and Engineering Research Council of Canada (through Discovery Grants to A. M.) for financial support during his residency in the graduate program. All CMIP5 model outputs used in this study are available via the ESGF peer-to-peer enterprise system site (https://esgf-node.llnl.gov/search/cmip5/). CaCO3 sediment contents and CCD distributions are available on the NOAA Ocean Carbon Data System website (https://www.nodc.noaa.gov/ocads/oceans/ndp_099/ndp099.html).

References

Adcroft, A., Hill, C., & Marshall, J. (1997). Representation of topography by shaved cells in a height coordinate ocean model. *Monthly Weather Review*, *125*, 2293–2315. https://doi.org/10.1175/1520-0493(1997)125<2293:ROTBSC>2.0.CO;2

Alexander, K., Meissner, K. J., & Bralower, T. J. (2015). Sudden spreading of corrosive bottom water during the Palaeocene–Eocene Thermal Maximum. *Nature Geoscience*, *8*(6), 458–461. https://doi.org/10.1038/ngeo2430

Anderson, L. G., Olsson, K., Jones, E. P., Chierici, M., & Fransson, A. (1998). Anthropogenic carbon dioxide in the Arctic Ocean: Inventory and sinks. *Journal of Geophysical Research*, *103*, 27,707–27,716. https://doi.org/10.1029/98JC02586

Archer, D. (1996). A data-driven model of the global calcite lysocline. *Global Biogeochemical Cycles*, *10*, 511–526. https://doi.org/10.1029/96GB01521

Archer, D., Eby, M., Brovkin, V., Ridgwell, A., Cao, L., Mikolajewicz, U., et al. (2009). Atmospheric lifetime of fossil fuel carbon dioxide. *Annual Review of Earth and Planetary Sciences*, *37*, 117–134. https://doi.org/10.1146/annurev.earth.031208.100206

Archer, D., Kheshgi, H., & Maier-Reimer, E. (1998). Dynamics of fossil fuel CO_2 neutralization by marine $CaCO_3$. *Global Biogeochemical Cycles*, *12*, 259–276. https://doi.org/10.1029/98GB00744

Archer, D. E., Morford, J. L., & Emerson, S. R. (2002). A model of suboxic sedimentary diagenesis suitable for automatic tuning and gridded global domains. *Global Biogeochemical Cycles*, *16*(1), 17-1–17-21. https://doi.org/10.1029/2000GB001288

Bates, N. R., Best, M. H. P., Neely, K., Garley, R., Dickson, A. G., & Johnson, R. J. (2012). Detecting anthropogenic carbon dioxide uptake and ocean acidification in the North Atlantic Ocean. *Biogeosciences*, *9*, 2509–2522. https://doi.org/10.5194/bg-9-2509-2012

Bellouin, N., Boucher, O., Haywood, J., Johnson, C., Jones, A., Rae, J., & Woodward, S. (2007. *Improved representation of aerosols for HadGEM2.* Meteorological Office Hadley Centre, Technical Note 73. https://doi.org/10.1029/2011jd016074

Berelson, W. M., Balch, W. M., Najjar, R., Feely, R. A., Sabine, C., & Lee, K. (2007). Relating estimates of $CaCO_3$ production, export, and dissolution in the water column to measurements of $CaCO_3$ rain into sediment traps and dissolution on the sea floor: A revised global carbonate budget. *Global Biogeochemical Cycles*, *21*. https://doi.org/10.1029/2006gb002803

Boudreau, B. P. (1996). A method-of-lines code for carbon and nutrient diagenesis in aquatic sediments. *Computers & Geosciences*, *22*(5), 479–496. https://doi.org/10.1016/0098-3004(95)00115-8

Boudreau, B. P. (2013). Carbonate dissolution rates at the deep ocean floor. *Geophysical Research Letters*, *40*, 744–748. https://doi.org/10.1029/2012GL054231

Boudreau, B. P., & Guinasso, N. L. Jr. (1982). The influence of a diffusive boundary layer on accretion, dissolution, and diagenesis at the sea floor. In K. A. Fanning & F. T. Manheim (Eds.), *The Dynamic Environment of the Ocean Floor* (pp. 115–145). Lexington: Lexington Books. https://doi.org/10.1029/2012gl054231

Boudreau, B. P., & Jørgensen, B. B. (2001). *The benthic boundary layer: Transport processes and biogeochemistry*. Oxford: Oxford University Press. https://doi.org/10.1029/01eo00381

Boudreau, B. P., & Luo, Y. (2017). Retrodiction of secular variations in deep-sea CaCO 3 burial during the Cenozoic. *Earth and Planetary Science Letters*, *474*, 1–12. https://doi.org/10.1016/j.epsl.2017.06.005

Boudreau, B. P., Middelburg, J. J., Hofmann, A. F., & Meysman, F. J. R. (2010). Ongoing transients in carbonate compensation. *Global Biogeochemical Cycles*, *24*. https://doi.org/10.1029/2009GB003654

Boudreau, B. P., Middelburg, J. J., & Luo, Y. (2018). The role of calcification in carbonate compensation. *Nature Geoscience*, *11*, 894–900. https://doi.org/10.1038/s41561-018-0259-5

Boudreau, B. P., Middelburg, J. J., & Meysman, F. J. R. (2010). Carbonate compensation dynamics. *Geophysical Research Letters*, *37*. https://doi.org/10.1029/2009GL041847

Bramlette, M. N. (1961). Pelagic sediments. In M. Sears (Ed.), *Oceanography* (Vol. 67, pp. 345–366). Publications of the American Association for the Advancement of Science.

Broecker, W. S., & Peng, T. H. (1982). *Tracers in the sea*. Lamont-Doherty Geological Observatory, Columbia University: Palisades, New York.

Bryan, F. O., Gent, P. R., & Thomas, R. (2014). Can Southern Ocean eddy effects be parameterized in climate models? *Journal of Climate*, *27*, 411–425. https://doi.org/10.1175/JCLI-D-12-00759.1

Caesar, L., Rahmstorf, S., Robinson, A., Feulner, G., & Saba, V. (2018). Observed fingerprint of a weakening Atlantic Ocean overturning circulation. *Nature*, *556*, 191–196. https://doi.org/10.1038/s41586-018-0006-5

Caldeira, K., & Wickett, M. E. (2003). Anthropogenic carbon and ocean pH. *Nature*, *425*, 365–365. https://doi.org/10.1038/425365a

Callies, J. (2018). Restratification of abyssal mixing layers by submesoscale baroclinic eddies. *Journal of Physical Oceanography*, *48*, 1995–2010. https://doi.org/10.1175/JPO-D-18-0082.1

Carter, B. R., Feely, R. A., Mecking, S., Cross, J. N., Macdonald, A. M., Siedlecki, S. A., et al. (2017). Two decades of Pacific anthropogenic carbon storage and ocean acidification along GO-SHIP sections P16 and P02. *Global Biogeochemical Cycles*. https://doi.org/10.1002/2016GB005485

Chen, C.-T. A. (1982). On the distribution of anthropogenic CO_2 in the Atlantic and Southern oceans. *Deep Sea Research*, *29*, 563–580. https://doi.org/10.1016/0198-0149(82)90076-0

Cheng, W., Chiang, J. C. H., & Zhang, D. (2013). Atlantic Meridional Overturning Circulation (AMOC) in CMIP5 models: RCP and historical simulations. *Journal of Climate*, *26*, 7187–7197. https://doi.org/10.1175/JCLI-D-12-00496.1

Ciais, P., Sabine, C., Bala, G., Bopp, L., Brovkin, V., Canadell, J., et al. (2013). Carbon and other biogeochemical cycles. In T. F. Stocker, D. Qin, G.-K. Plattner, M. Tignor, S. K. Allen, J. Boschung, A. Nauels, Y. Xia, V. Bex, & P. M. Midgley (Eds.), *Climate Change 2013: The Physical Science Basis. Contribution of Working Group I to the Fifth Assessment Report of the Intergovernmental Panel on Climate Change* (pp. 465–570). Cambridge, United Kingdom and New York, NY, USA: Cambridge University Press. https://doi.org/10.1017/cbo9781107415324.023

Collins, M., Knutti, R., Arblaster, J., Dufresne, J.-L., Fichefet, T., Friedlingstein, P., et al. (2013). Long-term Climate Change: Projections, Commitments and Irreversibility. In T. F. Stocker, D. Qin, G.-K. Plattner, M. Tignor, S. K. Allen, J. Boschung, A. Nauels, Y. Xia, V. Bex, & P. M. Midgley (Eds.), *Climate Change 2013: The Physical Science Basis. Contribution of Working Group I to the Fifth Assessment Report of the Intergovernmental Panel on Climate Change* (pp. 1029–1136). Cambridge, United Kingdom and New York, NY, USA: Cambridge University Press. https://doi.org/10.1017/CBO9781107415324.024

Collins, W. J., Bellouin, N., Doutriaux-Boucher, M., Gedney, N., Halloran, P., Hinton, T., et al. (2011). Development and evaluation of an Earth-System model—HadGEM2. *Geoscientific Model Development*, *4*, 1051–1075. https://doi.org/10.5194/gmd-4-1051-2011

Dade, W. B. (1993). Near-bed turbulence and hydrodynamic control of diffusional mass transfer at the sea floor. *Limnology and Oceanography*, *38*, 52–69. https://doi.org/10.4319/lo.1993.38.1.0052

de Lavergne, C., Madec, G., Roquet, F., Holmes, R. M., & McDougall, T. J. (2017). Abyssal ocean overturning shaped by seafloor distribution. *Nature*, *551*, 181–186. https://doi.org/10.1038/nature24472

de Lavergne, C., Palter, J. B., Galbraith, E. D., Bernardello, R., & Marinov, I. (2014). Cessation of deep convection in the open Southern Ocean under anthropogenic climate change. *Nature Climate Change*, *4*, 278–282. https://doi.org/10.1038/nclimate2132

Delworth, T. L., Rosati, A., Anderson, W., Adcroft, A. J., Balaji, V., Benson, R., et al. (2012). Simulated climate and climate change in the GFDL CM2.5 high-resolution coupled climate model. *Journal of Climate*, *25*, 2755–2781. https://doi.org/10.1175/JCLI-D-11-00316.1

Desbruyères, D. G., Purkey, S. G., McDonagh, E. L., Johnson, G. C., & King, B. A. (2016). Deep and abyssal ocean warming from 35 years of repeat hydrography. *Geophysical Research Letters*, *43*(19), 10,356–10,365. https://doi.org/10.1002/2016GL070413

Dickson, A. G. (1990). Standard potential of the reaction: $AgCl(s)+1/2H_2(g) = Ag(s)+HCl$ (aq), and the standard acidity constant of the ion HSO_4^- in synthetic sea water from 273.15 to 318.15 K. *The Journal of Chemical Thermodynamics*, *22*, 113–127. https://doi.org/10.1016/0021-9614(90)90074-Z

Dlugokencky, E., & Tans, P. (2018). *Trends in atmospheric carbon dioxide*. National Oceanic and Atmospheric Aministration, Earth System Research Laboratory (NOAA/ESRL). https://doi.org/10.1016/j.atmosenv.2008.12.028

Dufour, C. O., Morrison, A. K., Griffies, S. M., Frenger, I., Zanowski, H., & Winton, M. (2017). Preconditioning of the Weddell Sea Polynya by the ocean mesoscale and dense water overflows. *Journal of Climate*, *30*(19), 7719–7737. https://doi.org/10.1175/jcli-d-16-0586.1

Dufresne, J. L., Foujols, M. A., Denvil, S., Caubel, A., Marti, O., Aumont, O., et al. (2013). Climate change projections using the IPSL-CM5 Earth System Model: From CMIP3 to CMIP5. *Climate Dynamics*, *40*, 2123–2165. https://doi.org/10.1007/s00382-012-1636-1

Dunne, J. P., Hales, B., & Toggweiler, J. R. (2012). Global calcite cycling constrained by sediment preservation controls. *Global Biogeochemical Cycles*, *26*. https://doi.org/10.1029/2010gb003935

Dunne, J. P., John, J. G., Adcroft, A. J., Griffies, S. M., Hallberg, R. W., Shevliakova, E., et al. (2012). GFDL's ESM 2 Global Coupled Climate–Carbon Earth System Models. Part I: Physical formulation and baseline simulation characteristics. *Journal of Climate*, *25*, 6646–6665. https://doi.org/10.1175/JCLI-D-11-00560.1

Dunne, J. P., John, J. G., Shevliakova, E., Stouffer, R. J., Krasting, J. P., Malyshev, S. L., et al. (2013). GFDL's ESM 2 Global Coupled Climate–Carbon Earth System Models. Part II: Carbon system formulation and baseline simulation characteristics. *Journal of Climate*, *26*, 2247–2267. https://doi.org/10.1175/JCLI-D-12-00150.1

Dutkiewicz, A., Müller, R. D., O'Callaghan, S., & Jónasson, H. (2015). Census of seafloor sediments in the world's ocean. *Geology*, *43*, 795–798. https://doi.org/10.1130/G36883.1

Edmond, J. M. (1974). On the dissolution of carbonate and silicate in the deep ocean. *Deep Sea Research*, *21*, 455–480. https://doi.org/10.1016/0011-7471(74)90094-1

Egbert, G. D., & Erofeeva, S. Y. (2002). Efficient inverse modeling of barotropic ocean tides. *Journal of Atmospheric and Oceanic Technology*, *19*, 183–204. https://doi.org/10.1175/1520-0426(2002)019<0183:EIMOBO>2.0.CO;2

Eyre, B. D., Cyronak, T., Drupp, P., Carlo, E. H. D., Sachs, J. P., & Andersson, A. J. (2018). Coral reefs will transition to net dissolving before end of century. *Science*, *359*, 908–911. https://doi.org/10.1126/science.aao1118

Fassbender, A. J., Sabine, C. L., & Feifel, K. M. (2016). Consideration of coastal carbonate chemistry in understanding biological calcification. *Geophysical Research Letters*, *43*(9), 4467–4476. https://doi.org/10.1002/2016gl068860

Feely, R. A., Sabine, C. L., Lee, K., Millero, F. J., Lamb, M. F., Greeley, D., et al. (2002). In situ calcium carbonate dissolution in the Pacific Ocean. *Global Biogeochemical Cycles*, *16*, 91-1–91-12. https://doi.org/10.1029/2002GB001866

Fukuda, S. Y., Suzuki, Y., & Shiraiwa, Y. (2014). Difference in physiological responses of growth, photosynthesis and calcification of the coccolithophore Emiliania huxleyi to acidification by acid and CO_2 enrichment. *Photosynthesis Research*, *121*, 299–309. https://doi.org/10.1007/s11120-014-9976-9

Garner, S. T. (2005). A topographic drag closure built on an analytical base flux. *Journal of the Atmospheric Sciences*, *62*, 2302–2315. https://doi.org/10.1175/JAS3496.1

Gebbie, G., & Huybers, P. (2012). The mean age of ocean waters inferred from radiocarbon observations: Sensitivity to surface sources and accounting for mixing histories. *Journal of Physical Oceanography*, *42*, 291–305. https://doi.org/10.1175/JPO-D-11-043.1

Gent, P. R., & McWilliams, J. C. (1990). Isopycnal mixing in ocean circulation models. *Journal of Physical Oceanography*, *20*, 150–155. https://doi.org/10.1175/1520-0485(1990)020<0150:IMIOCM>2.0.CO;2

Griffies, S. M. (1998). The Gent–McWilliams skew flux. *Journal of Physical Oceanography*, *28*, 831–841. https://doi.org/10.1175/1520-0485(1998)028<0831:TGMSF>2.0.CO;2

Griffies, S. M., & Hallberg, R. W. (2000). Biharmonic friction with a Smagorinsky-like viscosity for use in large-scale eddy-permitting ocean models. *Monthly Weather Review*, *128*, 2935–2946. https://doi.org/10.1175/1520-0493(2000)128<2935:bfwasl>2.0.co;2

Griffies, S. M., Winton, M., Anderson, W. G., Benson, R., Delworth, T. L., Dufour, C. O., et al. (2015). Impacts on ocean heat from transient mesoscale eddies in a hierarchy of climate models. *Journal of Climate*, *28*, 952–977. https://doi.org/10.1175/JCLI-D-14-00353.1

Hales, B. (2003). Respiration, dissolution, and the lysocline. *Paleoceanography and Paleoclimatology*, *18*. https://doi.org/10.1029/2003PA000915

Hallberg, R. (2013). Using a resolution function to regulate parameterizations of oceanic mesoscale eddy effects. *Ocean Modelling*, *72*, 92–103. https://doi.org/10.1016/j.ocemod.2013.08.007

Hecht, M. W., & Hasumi, H. (2008). AGU Monograph. In M. W. Hecht & H. Hasumi (Eds.), *2008: Ocean modeling in an eddying regime*, *Geophys. Monogr.* (Vol. 177, 409 pp.). Amer. Geophys. Union. https://doi.org/10.1029/GM177

Heinze, C., Maier-Reimer, E., Winguth, A. M. E., & Archer, D. (1999). A global oceanic sediment model for long-term climate studies. *Global Biogeochemical Cycles*, *13*(1), 221–250. https://doi.org/10.1029/98GB02812

Heuzé, C., Heywood, K. J., Stevens, D. P., & Ridley, J. K. (2015). Changes in global ocean bottom properties and volume transports in CMIP5 models under climate change scenarios. *Journal of Climate*, *28*, 2917–2944. https://doi.org/10.1175/JCLI-D-14-00381.1

Higashino, M., & Stefan, H. G. (2004). Diffusive boundary layer development above a sediment-water interface. *Water Environment Research*, *76*, 292–300. https://doi.org/10.2175/106143004X141870

Huiskamp, W. N., & Meissner, K. J. (2012). Oceanic carbon and water masses during the Mystery Interval: A model-data comparison study. *Paleoceanography*, *27*. https://doi.org/10.1029/2012PA002368

Johnson, G. C. (2008). Quantifying Antarctic Bottom Water and North Atlantic Deep Water volumes. *Journal of Geophysical Research*, *113*. https://doi.org/10.1029/2007JC004477

Joos, F., & Spahni, R. (2008). Rates of change in natural and anthropogenic radiative forcing over the past 20,000 years. *Proceedings of the National Academy of Sciences*, *105*, 1425–1430. https://doi.org/10.1073/pnas.0707386105

Kendall, M. G. (1975). *Rank correlation methods*. London, UK: Charles Griffin. https://doi.org/10.2307/2333282

Khatiwala, S., Primeau, F., & Hall, T. (2009). Reconstruction of the history of anthropogenic CO_2 concentrations in the ocean. *Nature*, *462*, 346–349. https://doi.org/10.1038/nature08526

Körtzinger, A., Mintrop, L., & Duinker, J. C. (1998). On the penetration of anthropogenic CO_2 into the North Atlantic Ocean. *Journal of Geophysical Research*, *103*, 18,681–18,689. https://doi.org/10.1029/98JC01737

Krumhardt, K. M., Lovenduski, N. S., Long, M. C., Levy, M., Lindsay, K., Moore, J. K., & Nissen, C. (2019). Coccolithophore growth and calcification in an acidified ocean: Insights from Community Earth System model simulations. *Journal of Advances in Modeling Earth Systems*, *11*, 1418–1437. https://doi.org/10.1029/2018MS001483

Larkum, A. W. D., Koch, E. M. W., & Kühl, M. (2003). Diffusive boundary layers and photosynthesis of the epilithic algal community of coral reefs. *Marine Biology*, *142*, 1073–1082. https://doi.org/10.1007/s00227-003-1022-y

Lauvset, S. K., Key, R. M., Olsen, A., Heuven, S.v., Velo, A., Lin, X., et al. (2016). A new global interior ocean mapped climatology: the 1° × 1° GLODAP version 2. *Earth System Science Data*, *8*, 325–340. https://doi.org/10.5194/essd-8-325-2016

Le Quéré, C., Andrew, R. M., Friedlingstein, P., Sitch, S., Pongratz, J., Manning, A. C., et al. (2018). Global Carbon Budget 2017. *Earth System Science Data*, *10*, 405–448. https://doi.org/10.5194/essd-10-405-2018

Levich, V. G. (1962). *Physicochemical Hydrodynamics*. Prentice-Hall. https://doi.org/10.1149/1.2425619

Lorke, A., Müller, B., Maerki, M., & Wüest, A. (2003). Breathing sediments: The control of diffusive transport across the 530 sediment-water interface by periodic boundary-layer turbulence. *Limnology and Oceanography*, *48*, 2077–2085. https://doi.org/10.4319/lo.2003.48.6.2077

Luecke, C. A., Arbic, B. K., Bassette, S. L., Richman, J. G., Shriver, J. F., Alford, M. H., et al. (2017). The global mesoscale eddy available potential energy field in models and observations. *Journal of Geophysical Research, Oceans*, *122*, 9126–9143. https://doi.org/10.1002/2017JC013136

Lueker, T. J., Dickson, A. G., & Keeling, C. D. (2000). Ocean pCO_2 calculated from dissolved inorganic carbon, alkalinity, and equations for K_1 and K_2: Validation based on laboratory measurements of CO_2 in gas and seawater at equilibrium. *Marine Chemistry*, *70*, 105–119. https://doi.org/10.1016/S0304-4203(00)00022-0

MacGilchrist, G. A., Garabato, A. C. N., Brown, P. J., Jullion, L., Bacon, S., Bakker, D. C. E., et al. (2019). Reframing the carbon cycle of the subpolar Southern Ocean. *Science Advances*. *5*, eaav6410. https://doi.org/10.1126/sciadv.aav6410

Mackenzie, F., & Andersson, A. (2013). The marine carbon system and ocean acidification during Phanerozoic time. *Geochemical Perspectives*, 1–227. https://doi.org/10.7185/geochempersp.2.1

Mann, H. B. (1945). Nonparametric tests against trend. *Econometrica*, *13*, 245–259. https://doi.org/10.2307/1907187

Marshall, D. P., & Adcroft, A. J. (2010). Parameterization of ocean eddies: Potential vorticity mixing, energetics and Arnold's first stability theorem. *Ocean Modelling*, *32*, 188–204. https://doi.org/10.1016/j.ocemod.2010.02.001

Matsumoto, K. (2007). Radiocarbon-based circulation age of the world oceans. *Journal of Geophysical Research*, 112. https://doi.org/10.1029/2007JC004095

Maugendre, L., Gattuso, J.-P., Poulton, A. J., Dellisanti, W., Gaubert, M., Guieu, C., & Gazeau, F. (2017). No detectable effect of ocean acidification on plankton metabolism in the NW oligotrophic Mediterranean Sea: Results from two mesocosm studies. *Estuarine, Coastal and Shelf Science*, *186*(A), 89–99. https://doi.org/10.1016/j.ecss.2015.03.009

McDougall, T.J. and Barker, P.M. (2011) Getting started with TEOS-10 and the Gibbs Seawater (GSW) Oceanographic Toolbox. SCOR/IAPSO WG127, p. 28. https://doi.org/10.1016/j.ocemod.2015.04.002

McNeil, B. I., Matear, R. J., Key, R. M., Bullister, J. L., & Sarmiento, J. L. (2003). Anthropogenic CO_2 uptake by the ocean based on the global chlorofluorocarbon data set. *Science*, *299*, 235–239. https://doi.org/10.1126/science.1077429

Meijers, A. J. S. (2014). The Southern Ocean in the Coupled Model Intercomparison Project Phase 5. *Philosophical Transactions of the Royal Society A*, *372*, 20130296. https://doi.org/10.1098/rsta.2013.0296

Meinshausen, M., Smith, S. J., Calvin, K., Daniel, J. S., Kainuma, M. L. T., Lamarque, J. F., et al. (2011). The RCP greenhouse gas concentrations and their extensions from 1765 to 2300. *Climatic Change*, *109*, 213–241. https://doi.org/10.1007/s10584-011-0156-z

Mekik, F. A., Loubere, P. W., & Archer, D. E. (2002). Organic carbon flux and organic carbon to calcite flux ratio recorded in deep-sea carbonates: Demonstration and a new proxy. *Global Biogeochemical Cycles*, *16*. https://doi.org/10.1029/2001GB001634

Melet, A., Hallberg, R., Adcroft, A., Nikurashin, M., & Legg, S. (2015). Energy flux into internal Lee waves: sensitivity to future climate changes using linear theory and a climate model. *Journal of Climate*, *28*, 2365–2384. https://doi.org/10.1175/JCLI-D-14-00432.1

Menezes, V. V., Macdonald, A. M., & Schatzman, C. (2017). Accelerated freshening of Antarctic Bottom Water over the last decade in the Southern Indian Ocean. *Science Advances*, 3. https://doi.org/10.1126/sciadv.1601426

Meysman, F. J. R., Galaktionov, O. S., Gribsholt, B., & Middelburg, J. J. (2006). Bioirrigation in permeable sediments: Advective pore-water transport induced by burrow ventilation. *Limnology and Oceanography*, *51*, 142–156. https://doi.org/10.4319/lo.2006.51.1.0142

Millero, F. J. (1995). Thermodynamics of the carbon dioxide system in the oceans. *Geochimica et Cosmochimica Acta*, *59*, 661–677. https://doi.org/10.1016/0016-7037(94)00354-O

Millero, F. J. (2007). The marine inorganic carbon cycle. *Chemical Reviews*, *107*, 308–341. https://doi.org/10.1021/cr05557

Morozov, E. G., Demidov, A. N., Tarakanov, R. Y., & Zenk, W. (2010). *Deep water masses of the South and North Atlantic, abyssal channels in the Atlantic Ocean*. Dordrecht: Springer. https://doi.org/10.1007/978-90-481-9358-5_2

Morse, J. W., & Arvidson, R. S. (2002). The dissolution kinetics of major sedimentary carbonate minerals. *Earth-Science Reviews*, *58*, 51–84. https://doi.org/10.1016/S0012-8252(01)00083-6

Morse, J. W., Arvidson, R. S., & Lüttge, A. (2007). Calcium carbonate formation and dissolution. *Chemical Reviews*, *107*, 342–381. https://doi.org/10.1021/cr050358j

Morse, J. W., & Mackenzie, F. T. (1990). *Geochemistry of sedimentary carbonates*. Amsterdam: Elsevier. https://doi.org/10.1016/s0070-4571(08)70329-7

Mucci, A. (1983). The solubility of calcite and aragonite in seawater at various salinities, temperatures and one atmosphere total pressure. *American Journal of Science*, *283*, 780–799. http://doi.org/10.2475/ajs.283.7.780

Munhoven, G. (2007). Glacial–interglacial rain ratio changes: Implications for atmospheric CO_2 and ocean–sediment interaction. *Deep Sea Research Part II: Topical Studies in Oceanography*, *54*(5-7), 722–746. https://doi.org/10.1016/j.dsr2.2007.01.008

Naviaux, J. D., Subhas, A. V., Rollins, N. E., Dong, S., Berelson, W. B., & Adkins, J. F. (2019). Temperature dependence of calcite dissolution kinetics in seawater. *Geochimica et Cosmochimica Acta*, *246*, 363–384. https://doi.org/10.1016/j.gca.2018.11.037

Newsom, E. R., Bitz, C. M., Bryan, F. O., Abernathey, R., & Gent, P. R. (2016). Southern Ocean deep circulation and heat uptake in a high-resolution climate model. *Journal of Climate*, *29*, 2597–2619. https://doi.org/10.1175/JCLI-D-15-0513.1

Olsen, A., Key, R. M., van Heuven, S., Lauvset, S. K., Velo, A., Lin, X., et al. (2016). The Global Ocean Data Analysis Project version 2 (GLODAPv2)—An internally consistent data product for the world ocean. *Earth System Science Data*, *8*, 297–323. https://doi.org/10.5194/essd-8-297-2016

Orr, J. C., Epitalon, J.-M., Dickson, A. G., & Gattuso, J.-P. (2018). Routine uncertainty propagation for the marine carbon dioxide system. *Marine Chemistry*, *207*, 84–107. https://doi.org/10.1016/j.marchem.2018.10.006

Orr, J. C., Fabry, V. J., Aumont, O., Bopp, L., Doney, S. C., Feely, R. A., et al. (2005). Anthropogenic ocean acidification over the twenty-first century and its impact on calcifying organisms. *Nature*, *437*, 681–686. https://doi.org/10.1038/nature04095

Pearson, B., Fox-Kemper, B., Bachman, S. D., & Bryan, F. O. (2017). Evaluation of scale-aware subgrid mesoscale eddy models in a global eddy-rich model. *Ocean Modelling*, *115*, 42–58. https://doi.org/10.1016/j.ocemod.2017.05.007

Perez, F. F., Fontela, M., Garcia-Ibanez, M. I., Mercier, H., Velo, A., Lherminier, P., et al. (2018). Meridional overturning circulation conveys fast acidification to the deep Atlantic Ocean. *Nature*, *554*, 515–518. https://doi.org/10.1038/nature25493

Pérez, F. F., Mercier, H., Vázquez-Rodríguez, M., Lherminier, P., Velo, A., Pardo, P. C., et al. (2013). Atlantic Ocean CO_2 uptake reduced by weakening of the meridional overturning circulation. *Nature Geoscience*, *6*, 146–152. https://doi.org/10.1038/ngeo1680

Pierrot, D., Lewis, E., & Wallace, D. (2006). *MS Excel Program Developed for CO_2 System Calculations*. Oak Ridge, Tennessee: ORNL/CDIAC-105a, Carbon Dioxide Information Analysis Center, Oak Ridge National Laboratory, U.S. Department of Energy. https://doi.org/10.3334/cdiac/otg.co2sys_xls_cdiac105a

Pinsonneault, A. J., Matthews, H. D., Galbraith, E. D., & Schmittner, A. (2012). Calcium carbonate production response to future ocean warming and acidification. *Biogeosciences*, *9*(6), 2351–2364. https://doi.org/10.5194/bg-9-2351-2012

Purkey, S. G., & Johnson, G. C. (2010). Warming of global abyssal and deep Southern Ocean waters between the 1990s and 2000s: Contributions to global heat and sea level rise budgets. *Journal of Climate*, *23*, 6336–6351. https://doi.org/10.1175/2010JCLI3682.1

Purkey, S. G., & Johnson, G. C. (2013). Antarctic bottom water warming and freshening: Contributions to sea level rise, ocean freshwater budgets, and global heat gain. *Journal of Climate*, *26*, 6105–6122. https://doi.org/10.1175/JCLI-D-12-00834.1

Rhein, M., Kieke, D., Hüttl-Kabus, S., Roessler, A., Mertens, C., Meissner, R., et al. (2011). Deep water formation, the subpolar gyre, and the meridional overturning circulation in the subpolar North Atlantic. *Deep Sea Research Part II: Topical Studies in Oceanography*, *58*(17-18), 1819–1832. https://doi.org/10.1016/j.dsr2.2010.10.061

Riahi, K., Rao, S., Krey, V., Cho, C., Chirkov, V., Fischer, G., et al. (2011). RCP 8.5-A scenario of comparatively high greenhouse gas emissions. *Climatic Change*, *109*, 33–57. https://doi.org/10.1007/s10584-011-0149-y

Ridgwell, A., & Hargreaves, J. C. (2007). Regulation of atmospheric CO_2 by deep-sea sediments in an Earth system model. *Global Biogeochemical Cycles*, *21*. https://doi.org/10.1029/2006GB002764

Riley, J. P., & Tongudai, M. (1967). The major cation/chlorinity ratios in sea water. *Chemical Geology*, *2*, 263–269. https://doi.org/10.1016/0009-2541(67)90026-5

Ríos, A. F., Resplandy, L., García-Ibáñez, M. I., Fajar, N. M., Velo, A., Padin, X. A., et al. (2015). Decadal acidification in the water masses of the Atlantic Ocean. *Proceedings of the National Academy of Sciences of the United States of America*, *112*, 9950–9955. https://doi.org/10.1073/pnas.1504613112

Sabine, C. L., Feely, R. A., Key, R. M., Bullister, J. L., Millero, F. J., Lee, K., et al. (2002). Distribution of anthropogenic CO_2 in the Pacific Ocean. *Global Biogeochemical Cycles*, *16*, 30-31–30-17. https://doi.org/10.1029/2001GB001639

Santschi, P. H., Anderson, R. F., Fleisher, M. Q., & Bowles, W. (1991). Measurements of diffusive sublayer thicknesses in the ocean by alabaster dissolution, and their implications for the measurements of benthic fluxes. *Journal of Geophysical Research, Oceans*, *96*, 10,641–10,657. https://doi.org/10.1029/91JC00488

Santschi, P. H., Bower, P., Nyffeler, U. P., Azevedo, A., & Broecker, W. S. (1983). Estimates of the resistance to chemical transport posed by the deep-sea boundary layer. *Limnology and Oceanography*, *28*, 899–912. https://doi.org/10.4319/lo.1983.28.5.0899

Saynisch, J., Petereit, J., Irrgang, C., Kuvshinov, A., & Thomas, M. (2016). Impact of climate variability on the tidal oceanic magnetic signal—A model-based sensitivity study. *Journal of Geophysical Research, Oceans*, *121*, 5931–5941. https://doi.org/10.1002/2016JC012027

Schlichting, H. (1979). *Boundary layer theory*. New York: McGraw-Hill. https://doi.org/10.1007/978-3-662-52919-5_2

Smith, S. V., & Mackenzie, F. T. (2016). The role of $CaCO_3$ reactions in the contemporary CO_2 cycle. *Aquatic Geochemistry*, *22*(2), 153–175. https://doi.org/10.1007/s10498-015-9282-y

Steinberger, N., & Hondzo, M. (1999). Diffusional mass transfer at sediment-water interface. *Journal of Environmental Engineering*, *125*, 192–200. https://doi.org/10.1061/(ASCE)0733-9372(1999)125:2(192)

Steinfeldt, R., Rhein, M., Bullister, J. L., & Tanhua, T. (2009). Inventory changes in anthropogenic carbon from 1997-2003 in the Atlantic Ocean between 20°S and 65°N. *Global Biogeochemical Cycles*, *23*. https://doi.org/10.1029/2008GB003311

Sulpis, O., Boudreau, B. P., Mucci, A., Jenkins, C. J., Trossman, D. S., Arbic, B. K., & Key, R. M. (2018). Current $CaCO_3$ dissolution at the seafloor caused by anthropogenic CO_2. *Proceedings of the National Academy of Sciences*, *115*, 11700–11705. https://doi.org/10.1073/pnas.1804250115

Sulpis, O., Lix, C., Mucci, A., & Boudreau, B. P. (2017). Calcite dissolution kinetics at the sediment-water interface in natural seawater. *Marine Chemistry*, *195*, 70–83. https://doi.org/10.1016/j.marchem.2017.06.005

Teal, L. R., Bulling, M. T., Parker, E. R., & Solan, M. (2008). Global patterns of bioturbation intensity and mixed depth of marine soft sediments. *Aquatic Biology*, *2*, 207–218. https://doi.org/10.3354/ab00052

Thornalley, D. J. R., Oppo, D. W., Ortega, P., Robson, J. I., Brierley, C. M., Davis, R., et al. (2018). Anomalously weak Labrador Sea convection and Atlantic overturning during the past 150 years. *Nature*, *556*, 227–230. https://doi.org/10.1038/s41586-018-0007-4

Timko, P. G., Arbic, B. K., Richman, J. G., Scott, R. B., Metzger, E. J., & Wallcraft, A. J. (2013). Skill testing a three-dimensional global tide model to historical current meter records. *Journal of Geophysical Research, Oceans*, *118*(12), 6914–6933. https://doi.org/10.1002/2013jc009071

Trossman, D. S., Arbic, B. K., Garner, S. T., Goff, J. A., Jayne, S. R., Metzger, E. J., & Wallcraft, A. J. (2013). Impact of parameterized lee wave drag on the energy budget of an eddying global ocean model. *Ocean Modelling*, *72*, 119–142. http://doi.org/10.1016/j.ocemod.2013.08.006

Trossman, D. S., Arbic, B. K., Richman, J. G., Garner, S. T., Jayne, S. R., & Wallcraft, A. J. (2016). Impact of topographic internal lee wave drag on an eddying global ocean model. *Ocean Modelling*, *97*, 109–128. https://doi.org/10.1016/j.ocemod.2015.10.013

Tschumi, T., Joos, F., Gehlen, M., & Heinze, C. (2011). Deep ocean ventilation, carbon isotopes, marine sedimentation and the deglacial CO_2 rise. *Climate of the Past*, *7*(3), 771–800. https://doi.org/10.5194/cp-7-771-2011

van Cappellen, P., & Wang, Y. (1996). Cycling of iron and manganese in surface sediments; a general theory for the coupled transport and reaction of carbon, oxygen, nitrogen, sulfur, iron, and manganese. *American Journal of Science*, *296*(3), 197–243. https://doi.org/10.2475/ajs.296.3.197

van Heuven, S., Pierrot, D., Rae, J. W. B., Lewis, E., & Wallace, D. W. R. (2011). *MATLAB program developed for CO2 system calculations*. Oak Ridge, Tennessee: ORNL/CDIAC-105b. Carbon Dioxide Information Analysis Center, Oak Ridge National Laboratory, U.S. Department of Energy. https://doi.org/10.3334/CDIAC/otg.CO2SYS_MATLAB_v1.1

van Vuuren, D. P., Edmonds, J., Kainuma, M., Riahi, K., Thomson, A., Hibbard, K., et al. (2011). The representative concentration pathways: An overview. *Climatic Change*, *109*, 5–31. https://doi.org/10.1007/s10584-011-0148-z

Vázquez-Rodríguez, M., Touratier, F., Monaco, C. L., Waugh, D. W., Padin, X. A., Bellerby, R. G. J., et al. (2009). Anthropogenic carbon distributions in the Atlantic Ocean: Data-based estimates from the Arctic to the Antarctic. *Biogeosciences*, *6*, 439–451. https://doi.org/10.5194/bg-6-439-2009

Wallcraft, A. J., Kara, A. B., & Hurlburt, H. E. (2005). Convergence of Laplacian diffusion versus resolution of an ocean model. *Geophysical Research Letters*, *32*, L07604. https://doi.org/doi:10.1029/2005GL022514

Wanninkhof, R., Doney, S. C., Bullister, J. L., Levine, N. M., Warner, M., & Gruber, N. (2010). Detecting anthropogenic CO_2 changes in the interior Atlantic Ocean between 1989 and 2005. *Journal of Geophysical Research*, *115*. https://doi.org/10.1029/2010JC006251

Wanninkhof, R., Park, G.-H., Takahashi, T., Feely, R. A., Bullister, J. L., & Doney, S. C. (2013). Changes in deep-water CO_2 concentrations over the last several decades determined from discrete pCO_2 measurements. *Deep Sea Research Part I*, *74*, 48–63. https://doi.org/10.7916/D8QJ7T4F

Winton, M., Anderson, W. G., Delworth, T. L., Griffies, S. M., Hurlin, W. J., & Rosati, A. (2014). Has coarse ocean resolution biased simulations of transient climate sensitivity? *Geophysical Research Letters*, *41*, 8522–8529. https://doi.org/10.1002/2014GL061523

Woosley, R. J., Millero, F. J., & Wanninkhof, R. (2016). Rapid anthropogenic changes in CO_2 and pH in the Atlantic Ocean: 2003–2014. *Global Biogeochemical Cycles*, *30*, 70–90. https://doi.org/10.1002/2015GB005248

Wootton, J. T., Pfister, C. A., & Forester, J. D. (2008). Dynamic patterns and ecological impacts of declining ocean pH in a high-resolution multi-year dataset. *Proceedings of the National Academy of Sciences of the United States of America*, *105*(48), 18,848–18,853. https://doi.org/10.1073/pnas.0810079105

Zeebe, R. E. (2011). On the molecular diffusion coefficients of dissolved CO_2, HCO_3^-, and CO_3^{2-} and their dependence on isotopic mass. *Geochimica et Cosmochimica Acta*, *75*, 2483–2498. https://doi.org/10.1016/j.gca.2011.02.010

Zeebe, R. E., Ridgwell, A., & Zachos, J. C. (2016). Anthropogenic carbon release rate unprecedented during the past 66 million years. *Nature Geoscience*, *9*, 325–329. https://doi.org/10.1038/ngeo2681

Zhang, R. (2008). Coherent surface-subsurface fingerprint of the Atlantic meridional overturning circulation. *Geophysical Research Letters*, *35*. https://doi.org/10.1029/2008GL035463